A Comprehensive Study of Buoyant Confined Jets by Integrating Laboratory Experiments, CFD, and Machine Learning

Lingkun Meng

Thesis submitted to the University of Ottawa
in partial Fulfillment of the requirements for the
Master of Applied Science in Civil Engineering

Department of Civil Engineering
Academic Supervisors: Prof. Hossein Bonakdari, Prof. Abdolmajid Mohammadian
University of Ottawa

Abstract

This thesis presents a comprehensive study of the behavior and dispersion characteristics of vertically confined buoyant jets using an integrated approach combining laboratory experiments, computational fluid dynamics (CFD) and advanced machine learning techniques. The overall objective of this study is to accurately determine and predict the dynamic properties of buoyant jets under different confinement conditions in order to enhance the environmental management strategies for wastewater discharge systems.

In the experimental part, a laser-induced fluorescence (LIF) technique was used to capture the detailed concentration field of the buoyant jet. This method enables accurate visualization and quantification of the jet behavior under different flow scenarios characterized by varying degrees of lateral confinement, Froude number and Reynolds number. These experimental results provide a reliable benchmark for the validation of subsequent numerical simulations.

Numerical analysis using the open-source computational fluid dynamics (CFD) software OpenFOAM evaluates three commonly used Reynolds-averaged Navier-Stokes (RANS) turbulence models: the standard k-ε model, the RNG k-ε model, and the SST k-ω model. Among them, the standard k-ε model shows excellent predictive ability and is in high agreement with experimental observations. The model consistently has high coefficient of determination (R^2) and low normalized root mean square error (NRMSE), which proves its reliability in simulating complex buoyant jet phenomena.

To further improve the prediction accuracy and computational efficiency, three state-of-the-art machine learning models are employed in this study: Adaptive Neuro-Fuzzy Inference System (ANFIS), Extreme Learning Machine (ELM), and Multivariate Adaptive Regression Splines (MARS). The ELM model is efficient and maintains high accuracy, making it ideal for scenarios that require fast computation. MARS provides an interpretable framework that greatly facilitates the understanding of jet dynamics through explicit mathematical formulas derived from data-driven basis functions.

Overall, this integrated approach improves the accuracy of predictions of buoyant jet behavior and

is expected to significantly reduce the environmental impacts of wastewater management practices by enabling more informed decision making regarding the design and operation of wastewater discharge systems, ultimately supporting sustainable environmental management.

Acknoledgements

First and foremost, I would like to thank my supervisors, Prof. Abdolmajid Mohammadian and Prof. Hossein Bonakdari, for their patience, guidance, and constant encouragement throughout my studies and the writing of this thesis. They have always helped me find direction whenever I faced difficulties, and their expertise and advice have been invaluable to me.

I am grateful to Danial Goodarzi for the practical help and suggestions he provided during both the experimental work and the simulations, which made many parts of the process much smoother.

I am grateful to my parents, Jie Gao and Xiangfeng Meng, who have supported me for many years—not only caring for me in life but also providing financial support for over a decade, allowing me to focus on my studies without distraction.

I also thank my girlfriend, Shuyi Jia, for her support and encouragement in both life and studies. Her companionship and understanding have often been the reason I was able to keep going.

Finally, I would like to thank my friends and classmates, including Boxuan Chen, Dingyun Guo, and Zeyu Li, as well as my colleagues in the Hydraulics Laboratory, for their help, companionship, and cooperation. Whether through discussions about work, sharing daily life, or lending a hand when needed, they have all made this journey more enjoyable.

Table of Contents

List of Figures

List of Tables

List of Symbols

ρ_j	Jet density	kg / m^3
ρ_a	Test tank density	kg / m^3
t	Time	s
U_j	Jet velocity	m / s
t	Time	s
g	Gravity acceleration	m / s^2
g'	Specific gravitational acceleration	m / s^2
g_x, g_y, g_z	Gravitational acceleration components in x, y, and z directions	m / s^2
P	Pressure	Pa
Re	Jet Reynolds number	
Fr	Jet Froude number	
T_j	Jet temperature	$°C$
T_a	Test tank temperature	$°C$
ν	Kinematic viscosity	m^2 / s
ν_{eff}	Effective kinematic viscosity	m^2 / s
ν_t	Turbulent kinematic viscosity	m^2 / s
μ_t	Turbulent viscosity	m^2 / s
C_μ	dynamic viscosity	m^2 / s
S_{ij}	Generation of turbulent kinetic energy	
τ_{ij}	Stress component in j-direction on a plane normal to the i-axis	Pa
D	Nozzle diameter	mm
D_r	Riser tube diameter	mm
H_r	Riser tube height	mm
Y	Vertical distance from the jet nozzle	m
X	Horizontal distance from the centerline	m
k	Turbulent kinetic energy	m^2 / s^2
ε	Dissipation rate in $k{-}\varepsilon$ models	m^2 / s^3

ω	Specific dissipation rate	m^2 / s
η	Smoothing parameter	
ξ	Viscous term parameter	
C	Concentration	
$\widehat{C}$	Normalized concentration	
C_0	Inlet jet concentration	
C_a	Ambient concentration	
S	Dilution (C_0 / C)	
β	Confinement index	
α, β, γ	Empirical coefficients	
u, v, w	Velocity in the x, y, z direction, respectively	m / s
x, y, z	Coordinates	

List of Acronyms

CFD	Computational Fluid Dynamic
OpenFOAM	Open Field Operation And Manipulation
FVM	Finite Volume Method
LIF	Laser Induced Fluorescence
PIV	Particle Image Velocimetry
RANS	Reynolds-Averaged Navier-Stokes
LES	Large Eddy Simulation
DNS	Direct Numerical Simulation
PISO	Pressure-Implicit with Splitting of Operators
LRR	Launder-Reece-Rodi
RNG	Renormalized Group
SST	Shear Stress Transport
AI	Artificial Intelligence
ML	Mahcine Learning
SGGP	Single-Gene Genetic Programming
MGGP	Multi-Gene Genetic Programming
RF	Random Forest
VMD	Variational Mode Decomposition
LSE	Least Squares Estimation
ANN	Artificial Neural Network
ELM	Extreme Learning Machine
ANFIS	Adaptive Neuro Fuzzy Inference System
MARS	Multivariate Adaptive Regression Splines
SLFNN	Single-Hidden-Layer Feedforward Neural Network
RSS	Residual Sum of Squares
GCV	Generalized Cross-Validation
RMSE	Root Mean Squared Error
NRMSE	Normalized Root Mean Squared Error
MAE	Mean Absolute Error
MARE	Mean Absolute Relative Error

BF	Basis Functions

Chapter 1 Introduction

1.1 Background

Wastewater discharge management has become a growing environmental problem in recent decades, especially in coastal and urban riverine environments. Industrialization, urbanization and population growth have significantly increased the amount of wastewater discharged into natural water bodies (Schewe et al., 2014). Figure 1 illustrates two recent large-scale wastewater treatment initiatives in the Middle East to address these challenges. Among the various types of discharges, positively buoyant jets represent a common and complex phenomenon. The density of wastewater is lower than that of ambient water due to its elevated temperature or the presence of lighter dissolved substances. As the jet is injected into the ambient water system, the wastewater rises due to buoyancy and momentum and spreads out horizontally at the water surface. The behavior of these jets is influenced by several factors, including initial velocity, density differences, ambient water flow, and stratification (Jones et al., 2007; Zhang et al., 2016). Among the various factors, the effect of temperature on water density cannot be ignored. Within a certain range, density decreases with increasing temperature (Millero and Huang, 2009).

The environmental impacts of buoyant wastewater discharges are manifold, affecting aquatic ecosystems and water quality. High temperatures and chemical pollutants in discharges can harm aquatic organisms by altering habitats, disrupting reproductive cycles and causing physiological stress. At the same time, introducing nutrients and organic matter in effluents can lead to eutrophication, resulting in algal blooms and hypoxic conditions that further threaten aquatic biodiversity (Englert et al., 2013).

Studies of positively buoyant jets include a range of physical and computational approaches focusing on both near- and far-field behavior (Morelissen et al., 2016). Near-field analyses focus on the initial region of the jet, where mixing and momentum are dominated by the properties of the jet, while far-field analyses focus on broader dispersion patterns influenced by environmental conditions. Accurate modeling and predicting buoyant jet behavior requires integrating fluid dynamics principles, environmental engineering practices, and advanced numerical simulations. This is divided into three methods, experimental, integral, and simulation, to analyze the pipe's flow conditions and the jet's subsequent dispersion characteristics under different scenarios. This integrated approach will provide valuable insights into the optimal conditions for minimizing environmental impacts (Lee and Lee, 1998; Yan and Mohammadian, 2017). In this thesis, the near-field is mainly investigated.

In recent years, Computational Fluid Dynamics (CFD) has emerged as a powerful tool for analyzing the behavior of buoyant wastewater jets.The ability of CFD to visualize and quantify velocity fields, turbulence, and concentrations in detail compares favorably to experimental methods in terms of cost, flexibility, and the ability to simulate complex geometries and boundary conditions. By combining experimental data with CFD simulations, researchers can validate model accuracy and conduct parametric studies to optimize discharge design and minimize ecological impacts (Sina et al. 2025).

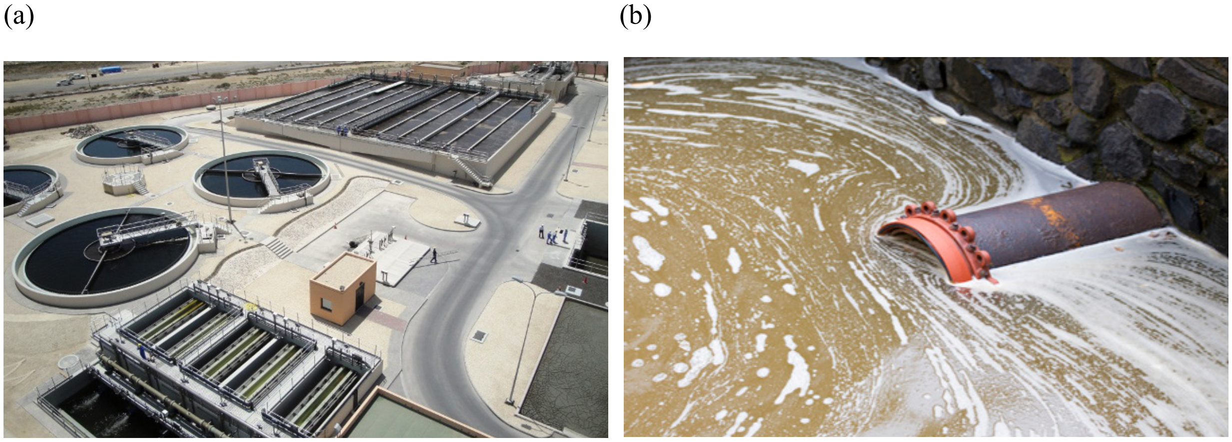

Figure 1.1. (a) Expansion project of the Tubli Wastewater Treatment Plant in Bahrain. From: https://www.utilities-me.com/suppliers/11738-bahrain-in-366mn-deal-to-expand-tubli-wastewater-treatment-plant (b)Sewer pipes in Saudi Arabia. From: https://www.utilities-me.com/news/7057-veolia-bags-aramcos-wastewater-treatment-deal

Confined jets are a common feature of various wastewater discharge terminals, attracting extensive research interest due to their complex flow dynamics and practical applications. This approach ensures that the pollutants are more evenly distributed and diluted, thereby reducing their environmental impact. The controlled nature of confined jets allows for better management of flow dynamics, including the initial velocity, direction, and turbulence, which are essential for effective wastewater treatment. Numerous studies have provided valuable data on local concentration distribution, inlet velocity profiles, and static pressure variations.

In addition, vertical variations in centerline dilution can be easily observed using the laser-induced fluorescence (LIF) experimental technique, resulting in a comprehensive dataset on laterally confined buoyant jets (Lee and Lee, 1998, Shinneeb et al., 2011). This extensive data collection has also allowed a detailed assessment of the impacts of wastewater discharge and dispersion processes on ambient waters.

1.2 Objectives of the study

The primary objective of this study is to investigate the behavior of buoyant jets with varying diameters, temperatures, and density characteristics discharged into an ambient fluid under different environmental and hydrodynamic conditions. The ultimate goal is to determine the optimal discharge configuration that minimizes environmental impact, particularly in terms of thermal and chemical stratification in receiving water bodies. To achieve this overarching aim, the study is structured around the following specific objectives:

- Using the open-source CFD software OpenFOAM, evaluate the accuracy and robustness of numerical models for simulating confined buoyant jets released near the bottom of a water column. This includes examining mesh sensitivity, boundary conditions, and solver settings. In addition to serving as a validation tool, CFD modeling provides an effective alternative for studying jet behavior when laboratory experiments are not feasible due to cost, scale, or facility limitations.
- Identify and implement the most suitable multiphase and turbulence models to simulate positively buoyant jets, accurately representing jet behavior, plume rise, mixing processes, and entrainment phenomena.
- Validate the selected numerical approach with experimental data, using advanced laboratory techniques such as Laser-Induced Fluorescence (LIF) to capture the spatial and temporal evolution of the buoyant plume. This ensures that the simulations replicate key physical processes and improve model reliability.
- Integrate machine learning techniques to analyze and interpret simulation and experimental results, with the aim of improving prediction accuracy, identifying hidden patterns, and supporting the development of data-driven surrogate models for faster and more efficient environmental assessments.

To fulfill these objectives, a series of three-dimensional numerical simulations of buoyant jet discharges were carried out using OpenFOAM. The study focused on modeling jets with different thermal and density properties under varied stratification and ambient flow scenarios. Simultaneously, physical experiments were conducted in a controlled laboratory environment, where LIF was employed to visualize and quantify the mixing and dispersion characteristics of the jets. Chapter 2 provides a detailed account of the numerical modeling framework, experimental setup, and validation methodology adopted in this study.

1.3 Novelty of the Study

This study evaluates the behavior of confined buoyant jets by combining detailed experimental work with state-of-the-art numerical simulations and makes some innovative contributions. Previous studies of vertical buoyant jets have usually been limited to qualitative analysis or have focused on only one approach in simulation or experiment. The application of such single methods may lead to high uncertainties, increased costs and sub-optimal results. By integrating experiments and numerical simulations, this study ensures a comprehensive analysis, enables cross-validation and improves the accuracy of results. This study provides clear guidance on selecting the best model for accurate and reliable predictions by comparing experimental data and numerical simulations of different turbulence models.

In addition, the study utilizes the powerful open-source Computational Fluid Dynamics (CFD) software OpenFOAM to perform extensive simulations of confined buoyant jets under various environmental conditions. Novel experimental techniques, such as laser-induced fluorescence (LIF), provide precise visualization of the jet behavior and ensure accurate and reliable validation of the numerical models. Furthermore, this study introduces a comprehensive framework that integrates experiments, CFD modeling, and machine learning techniques. This multi-method approach not only enhances the robustness of the analysis but also improves predictive performance. The behavior of constrained buoyant jets with different diameters, temperatures, and densities is investigated to identify optimal discharge configurations that minimize environmental impacts.

1.4 Organization of thesis

This thesis consists of five chapters as detailed below: Chapter 1 provides an introduction. Chapter 2 presents a comprehensive experimental and numerical presentation of a positive buoyancy confined jet, including data from experiments and numerical simulations. This chapter also discusses different turbulence models and results for incompressible fluids in simulations. Chapter 3 utilizes the prediction of the experiments through different machine learning tools so that the most appropriate AI model can be identified. Chapter 4 presents the conclusions and suggests directions for future research.

Chapter 2 experimental and CFD study of vertical confined buoyant jet

2.1 Introduction and literature review

2.1.1 Introduction

Confined buoyant jets are characterized by the interaction between the jet fluid and confined boundaries, which significantly alters the flow dynamics of the jet compared with unconfined jets. The presence of these boundaries affects the mixing, turbulence, and dilution processes, leading to complex flow patterns that are important for the mixing efficiencies of different types of flows. The study of these jets involves examining how factors such as the initial velocity, density differences, temperature variations, and environmental conditions affect their behavior.

As mentioned previously, confined positively buoyant jets, such as wastewater treatment and power plant cooling systems, are commonly used in various industrial and environmental discharge applications. These jets are released into the receiving water body with sufficient momentum to rise due to their positive buoyancy. At the discharge point, the initial jet momentum and buoyancy forces cause the jet to ascend. As the jet rises, it spreads laterally and mixes with ambient water, enhancing the dilution of the discharged effluent. The presence of confining boundaries significantly influences the behavior of the jet by altering its flow dynamics, creating complex interactions that can further enhance the mixing efficiency (Fig. 2.1). The vertical and lateral confinement of the jet affect its trajectory, turbulence, and mixing characteristics.

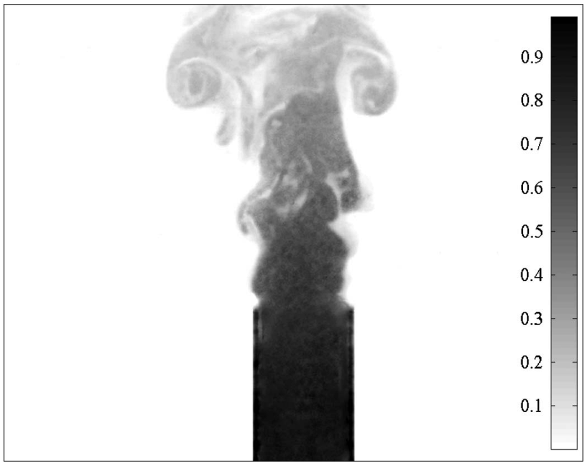

Fig. 2.1. Positively buoyant jet experiment diagram. From Yan and Mohammadian (2017)

2.1.2 Experimental Studies

Research on buoyant jets dates back to decades, with early studies focusing on qualitative observations and basic measurements. Early researchers used simple visualization techniques using dyes and documented them using photography to observe the trajectory and spread of buoyant jets. These initial experiments laid the groundwork for more in-depth research through key parameters, such as initial velocity, density differences, and the effect of environmental conditions on jet behavior.

Jirka and Harleman (1979) were among the first to experimentally study positive-buoyancy jets. They studied the stability and mixing characteristics of positive-buoyancy jets at confined depths. Their studies showed that the stability of these jets is affected by the interaction between the buoyant jet, surface impacts, and internal hydrodynamic jump regions. Under specific conditions of low buoyancy and shallow depth, the jets may become unstable, leading to the formation of recirculation cells. Wright's (1984) study of buoyant jets in a density-stratified crossflow presented a comprehensive approach for analyzing the behavior of these jets using a length-scale approach. The experimental results of this study emphasize that a simple power-law relationship is effective in estimating the rise height and dilution of buoyant jets in stratified environments when coefficient variability is considered, which are not universal constants but vary with parameters like the initial momentum and buoyancy fluxes, crossflow velocity, and stratification strength, reflecting the complex interaction between jet and ambient conditions. Gosman and Simitovic (1986) conducted a detailed experimental study of mixing in confined jets (Fig. 2.2) by measuring the local concentration distributions, inlet velocity distributions, and static pressure variations. However, their study did not examine vertically confined water jets.

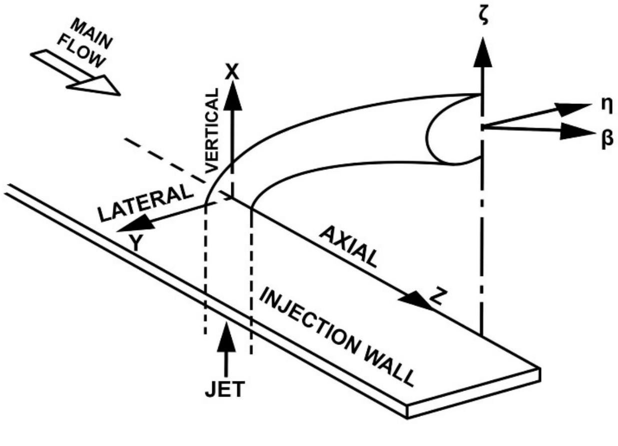

Fig. 2.2. Sketch of free buoyant jet flow pattern. From Gosman and Simitovic (1986)

In addition, due to technical and other limitations, the above cases all assume that the free buoyancy jet is not affected by any boundary dynamics, and there are almost no complete and in-depth experimental cases, most of which are qualitative analyses.

Ferrier et al. (1993) provided a comprehensive overview of the application of planar laser-induced fluorescence (PLIF) (Fig. 2.3) to the study of stratified fluids, highlighting that PLIF can provide accurate and detailed data for the visualization and measurement of jets.

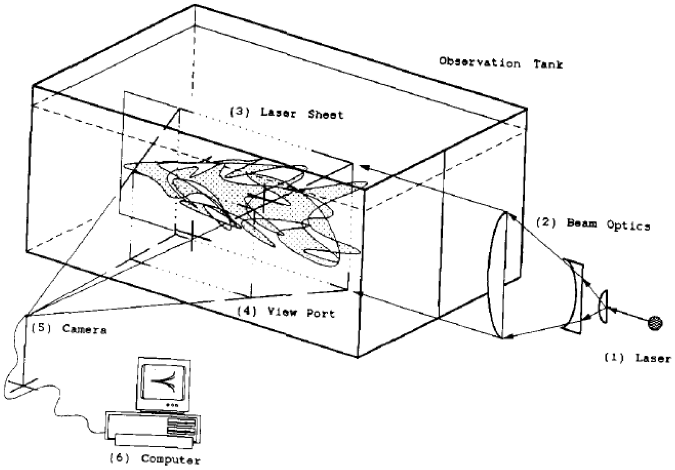

Fig. 2.3. Laser-induced fluorescence experimental set-up. From Ferrier et al. (1993)

Lee and Lee (1998) conducted a pivotal study to investigate the effect of lateral confinement on the initial dilution of a vertical circular buoyant jet. Their study utilized the Laser-Induced Fluorescence (LIF) technique and found that lateral confinement significantly affects the dilution behavior of the jet (Fig. 2.4). Their findings indicated that higher confinement indices result in minimal dilution within the riser, producing a top-hat concentration profile at the exit. In contrast, moderate confinement enhances mixing by increasing the turbulence and interaction with the enclosure. Coolen et al. (1999) investigated the application of laser-induced fluorescence (LIF) for the measurement of temperature in water using a neodymium laser.

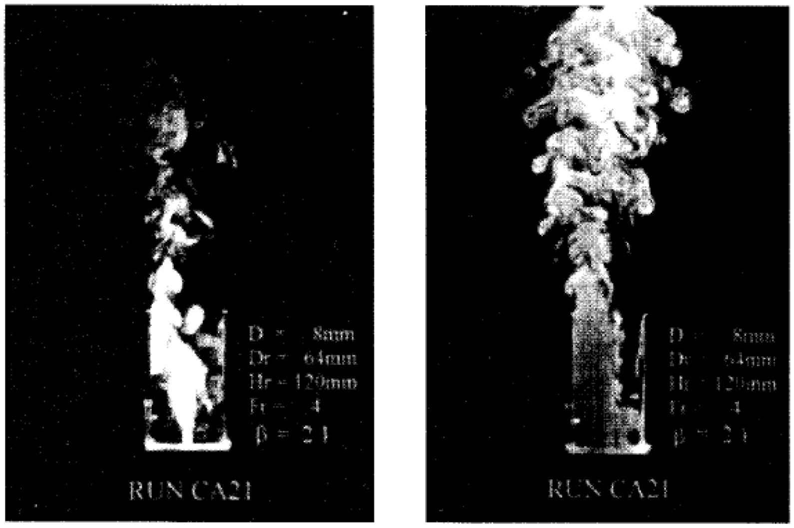

Fig. 2.4. Mixing pattern in central plane of unstable confined buoyant jet. From Lee and Lee (1998)

Pantzlaff and Lueptow (1999) studied the phenomenon of positive buoyancy jets, where the jet, driven by momentum and buoyancy, penetrates a free surface and stratifies above the bulk liquid. Their experiments using flow visualization and PIV showed that the penetration depth and time scale are related to the buoyancy flux and jet flow volume. Although this study focused on free jets rather than laterally confined jets, it is one of the first to provide detailed images of positively buoyant jets (Fig. 2.5).

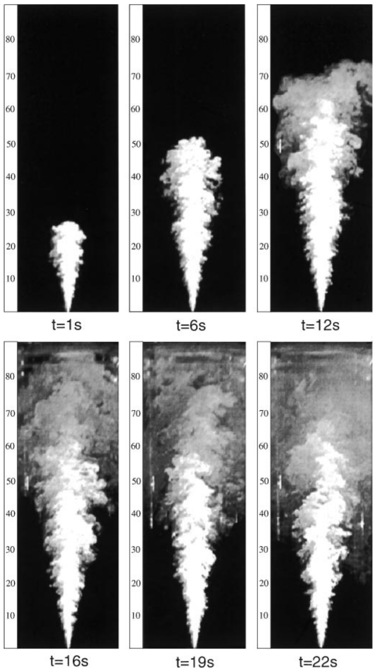

Fig. 2.5. Flow visualization of a positively buoyant jet. From Pantzlaff and Lueptow (1999)

Shinneeb et al. (2011) focused on the effects of vertical constraints on shallow water jets and highlighted the significant changes in the velocity distribution and turbulence structure. Their experiments, measured in detail using Particle Image Velocimetry (PIV), showed that vertical confinement suppressed entrainment, altered the mean velocity distribution, and displayed a more uniform velocity distribution with increasing downstream distance. This study provided important insights into the behavior of confined jets and emphasized on the importance of understanding confinement effects for applications involving shallow water discharges.

In brief, traditional methods such as photographs and shadowgraphs may produce subjective errors. Therefore, modern techniques, such as laser-induced fluorescence (LIF), particle image velocimetry (PIV), and particle tracking velocimetry (PTV), are becoming increasingly popular among researchers in jet studies. These advanced methods can not only accurately measure the concentration and motion trajectories to improve the accuracy and depth of flow analysis but also reduce the subjective uncertainty of experiments, enabling a more accurate and detailed understanding of jet behavior. Among these techniques, this study mainly uses the laser-induced fluorescence (LIF) method.

2.1.3 Numerical simulations

Although integral models are fast and inexpensive for describing turbulent buoyant jets, they are not as accurate in complex flows because of the simplification of many details, and they do not adequately capture some of the observed mixing features such as dilute mixing processes.

Computational fluid dynamics (CFD) methods are increasingly used in numerical simulations because they can accurately simulate complex fluid behaviors that are difficult to capture in physical experiments. They are also cost-effective, reduce the need for extensive physical setups, and enable rapid design iteration. Combining numerical simulations with experiments helps to validate the overall effect, thereby accurately optimizing the design to improve applications in industry and environmental management.

Turbulent jets are modeled by solving the Navier-Stokes equations, and CFD simulations involve various methods, such as direct simulation (DNS), large eddy simulation (LES), and Reynolds-averaged Navier-Stokes (RANS). Among them, LES and RANS methods are the most common types of turbulence modeling. In this study, several common RANS and LES models are used, which will be elaborated in the next section.

El-Amin et al. (2010) analyzed the compositions of unheated and heated turbulently confined jets using a realizable k–ε turbulence model. This study involved numerical simulation of a symmetric vertical hot water jet entering a cylindrical tank (Fig. 2.6). The simulations covered unsteady flow and analyzed the velocity, pressure, temperature, and turbulence distributions inside the tank. To validate the CFD simulation results, an experiment was conducted to measure the temperature of the system, which showed a good agreement between the measured and simulated temperatures.

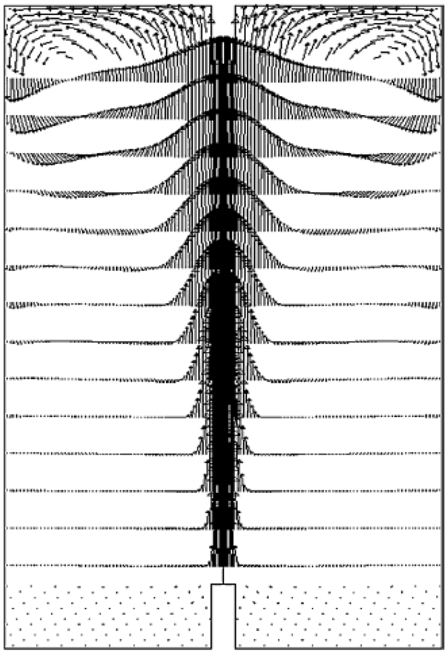

Fig. 2.6. Vectors of the axial velocity in the domain at t = 5 min, simulated results. From El-Amin et al. (2010)

Gildeh et al. (2015) conducted a comprehensive numerical study of the behavior of buoyant wall jets using various RANS turbulence models with the OpenFOAM software including k-ε, k-ω, and Reynolds Stress Model (RSM) to name a few, to simulate the behavior of buoyant wall jets discharging from submerged drainage outlets. This study aimed to determine the most accurate turbulence model for predicting flow dynamics, including attachment length, plume trajectory, temperature dilution, and velocity distribution. The simulations were subsequently validated against experimental and numerical data, showing that the realizable k–ε and Launder-Reece-Rodi (LRR) models provided the best performance.

Yan and Mohammadian (2017) provided a comprehensive analysis of the near-field flow and mixing characteristics of vertically discharging buoyant jets, subject to lateral constraints. The study was simulated using OpenFOAM CFD software with standard and buoyancy-modified k–ε turbulence models, and the results were validated against previous experimental data. This study demonstrated the accuracy and importance of the k–ε model in predicting the behavior of confined buoyant jets and in the environmental impact assessment and optimal design of wastewater discharge systems.

2.2 Methodology

Based on the research status in the above literature review, a systematic comparative study of different turbulence models is needed, especially for wastewater environments with different temperatures, which are very common in practice.

Fluid flow processes are studied using both experimental studies and numerical modeling. Experimental studies provide direct access to reliable physical information, but laboratory experiments are often costly and difficult to implement at the site. While scaling models can reduce the experimental difficulty, scaling errors and measurement errors under complex flow conditions, such as turbulence, may affect the accuracy of the results and require normalized analysis.

In contrast, numerical modeling is based on mathematical methods that simulate the fluid flow processes. With the computational power of advanced computers, actual physical conditions are simulated and verified with experimental data to provide a detailed and systematic analysis. Numerical simulations not only compensate for the limitations of experimental studies but also explore fluid behavior over a wider range of parameters (e.g., velocities), making it an important tool in the study of flow problems.

In this study, all experiments were conducted using a single jet nozzle with a fixed diameter of 6 mm. The effects of confinement were investigated by varying the diameters of the surrounding riser pipes and adjusting other flow parameters. In the numerical simulations, three groups of riser configurations with two different diameters were tested based on the 6 mm jet, and three turbulence models were applied for each configuration, resulting in a total of nine simulation cases.

The experiments were carried out for the centerline concentration and jet diffusion, in which the concentration and diffusion could be easily captured and analyzed by the camera. Numerical simulations provide a large number of jet parameters, including concentration, diffusion, and velocity. Due to the limitations of the experimental conditions, in the numerical simulation, we only analyzed the concentration and diffusion cases for comparison.

2.2.1 Experimental and computational parameters

One of the key points of the study is the determination of the concentration distribution across different cases by varying the Froude number (Fr), Reynolds number (Re), and outer riser tube diameter (Dr), while analyzing the jet behavior along the vertical direction. Here, Y denotes the vertical distance from the jet nozzle, and all vertical locations are expressed in the dimensionless form Y/D, where D is the nozzle diameter. In the experiments, data were collected starting from Y/D = 45, which corresponds to the lowest position with meaningful data, as closer regions were strongly influenced by the pipe wall (Yan and Mohammadian, 2017). Due to the height limitation of the test tank, measurements were restricted to a maximum of Y/D = 90. In Yan and Mohammadian's (2017) study, the normalized concentration at Y/D = 20 was used as the reference value of 1. In the present study, the same normalization approach was adopted; however, due to the use of multiple riser diameters (Dr) and riser heights (Hr), the reference concentration was taken at the jet orifice (Y = 0) to provide a consistent and objective basis for comparison across different configurations.

For experimental purposes, some of the key parameters used in this study are summarized in Table 2.1. A schematic diagram of the experimental setup, is shown in Figure 2.7 to provide a clear visual reference for the experimental design.

Table 2.1. Experimental and simulation parameters.

Parameter	Formula	Value
Jet Froude number	$Fr = U_j / \sqrt{g' D}$	20, 35
Jet Reynolds number	$\mathrm{Re} = U_j D / v$	2358, 3537
Jet velocity	U_j	0.393, 0.58

Jet temperature	T_j	37.19, 41.78 $^{\circ}C$
Jet reduced gravity	$g' = g\dfrac{\rho_j}{\rho_j - \rho_a}$	0.047, 0.064 m/s^2
Jet density	ρ_j	991.55, 993.29 kg/m^3
Test tank temperature	T_a	22 $^{\circ}C$
Test tank density	ρ_a	998.1 kg/m^3
Water kinematic viscosity	ν	$10^{-6} m^2/s$
Nozzle diameter	D	6 mm
Riser tube diameter	D_r	18, 31 mm
Confinement parameter	Y/D	45 - 90
Pipe diameter ratio	D_r/D	3, 5.16
Imager spatial resolution	Pixel(width)× Pixel(length)	1080×1920

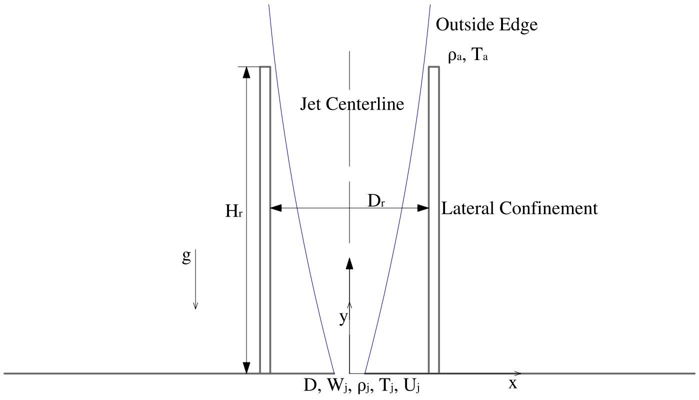

Fig. 2.7. Schematic diagram of a vertical buoyant jet subject to lateral constraints.

2.2.2 Experimental setup

The experiments were conducted in the Hydraulics Laboratory at the University of Ottawa, which was equipped with a test tank, constant pressure tank, and laser light source. Figure 2.8 illustrates the equipment setups. The test tank was made of glass and measured 3 m in length, 1.2 m in width, and 1 m in height, with a silicone hose with a flow meter and a switch in the middle of the hose from the constant pressure tank to the outlet pipe. The outlet pipe was a smooth polyvinyl chloride (PVC) pipe with an inner diameter of 6 mm. To achieve the set conditions, holes were punched in the lower side of the riser pipe for the hose and outlet pipes to be threaded through, and the outlet pipe was fixed in the center using 3D printing of the desired holes. In the direction of camera irradiation, a black light-blocking wooden plate was placed at the back of the pipe to prevent radium light from being reflected in the test tank and affecting the data. The flow at the outlet of the pipe was maintained by a constant-pressure tank located above the test tank (Fig. 2.8(a)), which maintained a constant head and fixed the flow rate to remain constant using a flow meter. The tank was fed by a hot fluorescent water tank located below it, and a storage tank was used to pump the hot fluorescent water. A small mixing pump and two heaters were installed in the tank to agitate and heat the solution to a stable and suitable temperature, which was then pumped upward. The density and temperature of the hot fluorescent and fresh water in the constant-pressure tanks and test tanks were measured and monitored using Anton Paar's portable densitometer DMA 35. After each experiment, the test tanks were emptied to ensure that no fluorescent contamination in the water would affect the subsequent experiments.

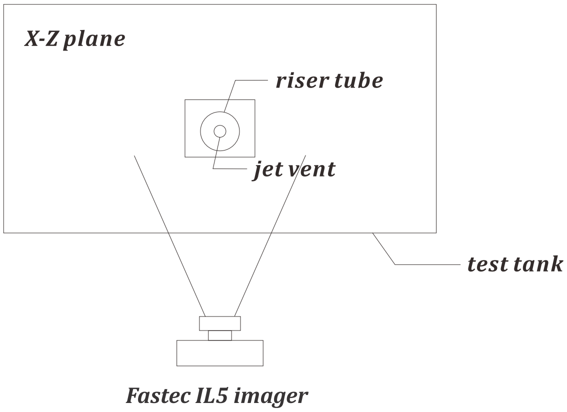

(a)

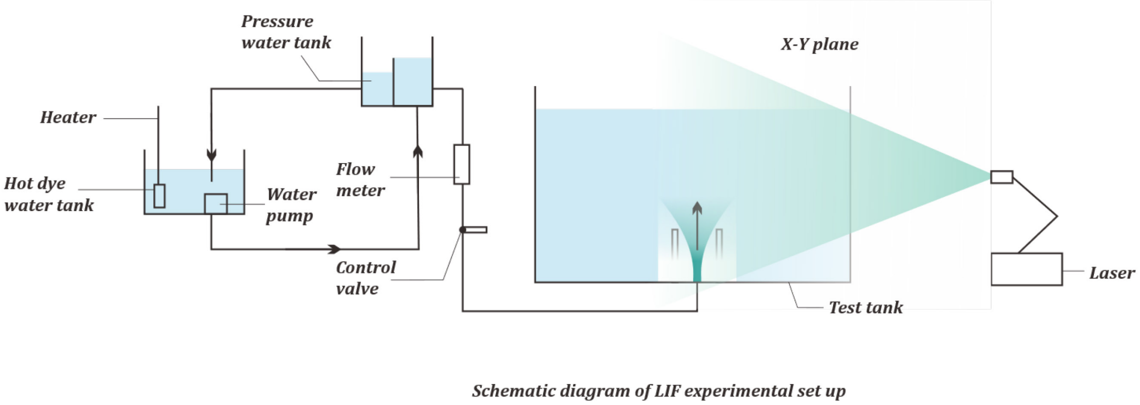

(b)

Figure 2.8. Schematic view of the experimental facility from (a) top view, and (b) side view.

Experiments were performed using the planar laser-induced fluorescence (LIF) technique to capture the two-dimensional concentration distribution in the jet. A small amount of the fluorescent dye rhodamine 6G was introduced into the jet fluid at a constant concentration, as suggested in previous studies by (Tian and Roberts, 2003; Sina et al. 2025). During the experiments, the vertical plane at the center of the jet nozzle was illuminated by a very thin laser sheet generated by a DPSS Microvec laser, which was used in continuous wave mode with 4 W of power and a wavelength of 532 nm. Fluid flow images were captured using a FASTEC IL5 camera equipped with a Nikon lens (1080 × 1920 pixels) and a high-speed CMOS imaging sensor. The compatibility of the camera with very low-light environments allowed for an exposure time of 2 ms in 8-bit grayscale mode. A total of 3782 photographs were taken at a rate of 50 frames per second for each experiment.

The reference point was at the position of the departure of the water jet. Concentration averaging was performed on the pictures taken to obtain the concentration contours, which can be used for comparison at a later stage. For post-processing, all the steps were written in a Python code to process the images, and several steps were carried out to obtain the required comparable contours, as shown in Figure 2.9. Due to the limitations of the laser, there are some false scan lines in the photographs taken, which are obvious in the averaging, but the small number of points in the data does not affect the results. In LIF measurements, due to the physical properties of the laser, the thickness of the laser is roughly 2 mm, and the camera is used to take images of the x-y plane.

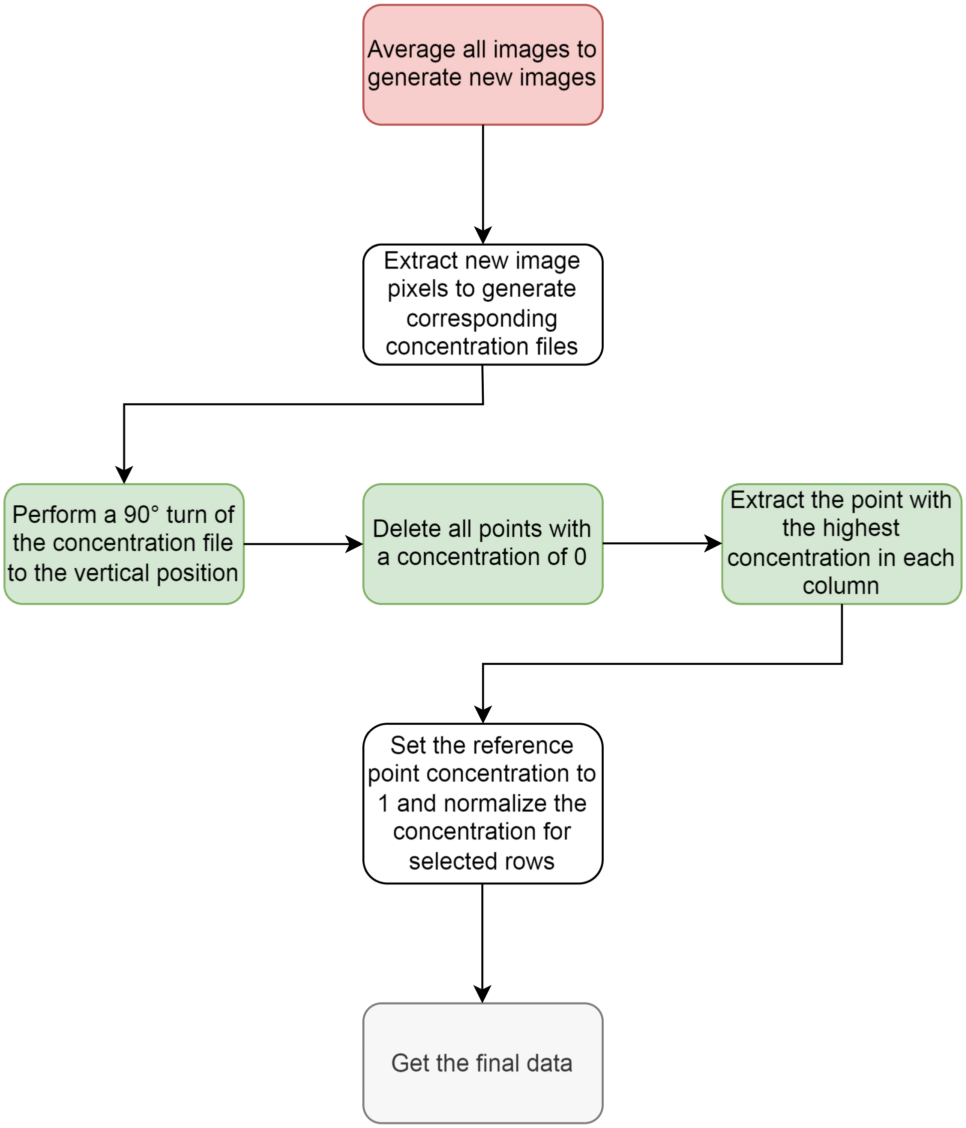

Figure 2.9. Flowchart of experimental image post-processing

2.2.3 Hydrodynamic equations

The model used was based on solver "pimpleFoam" in OpenFOAM. A temperature-dependent density term was added to the "pimpleFoam" solver to solve the three-dimensional Reynolds-averaged Navier-Stokes equations (RANS).

The general form of the equation can be expressed as (Imanian & Mohammadian, 2019):
Continuity:

$$\frac{\partial u}{\partial x}+\frac{\partial v}{\partial y}+\frac{\partial w}{\partial z}=0 \tag{2.1}$$

Momentum in the x-direction:

$$\frac{\partial u}{\partial t}+u\frac{\partial u}{\partial x}+v\frac{\partial u}{\partial y}+w\frac{\partial}{\partial z}=-\frac{1}{\rho}\frac{\partial P}{\partial x}+\frac{\partial}{\partial x}\left(v_{eff}\left(\frac{\partial u}{\partial x}\right)\right)+\frac{\partial}{\partial y}\left(v_{eff}\left(\frac{\partial u}{\partial y}\right)\right)+\frac{\partial}{\partial z}\left(v_{eff}\left(\frac{\partial u}{\partial z}\right)\right) \tag{2.2}$$

Momentum in the y-direction:

$$\frac{\partial u}{\partial t}+u\frac{\partial u}{\partial x}+v\frac{\partial u}{\partial y}+w\frac{\partial}{\partial z}=-\frac{1}{\rho}\frac{\partial P}{\partial y}+\frac{\partial}{\partial x}\left(v_{eff}\left(\frac{\partial v}{\partial x}\right)\right)+\frac{\partial}{\partial y}\left(v_{eff}\left(\frac{\partial v}{\partial y}\right)\right)+\frac{\partial}{\partial z}\left(v_{eff}\left(\frac{\partial v}{\partial z}\right)\right)-g\frac{\rho-\rho_0}{\rho} \tag{2.3}$$

Momentum in the z-direction:

$$\frac{\partial u}{\partial t}+u\frac{\partial u}{\partial x}+v\frac{\partial u}{\partial y}+w\frac{\partial}{\partial z}=-\frac{1}{\rho}\frac{\partial P}{\partial z}+\frac{\partial}{\partial x}\left(v_{eff}\left(\frac{\partial w}{\partial x}\right)\right)+\frac{\partial}{\partial y}\left(v_{eff}\left(\frac{\partial w}{\partial y}\right)\right)+\frac{\partial}{\partial z}\left(v_{eff}\left(\frac{\partial w}{\partial z}\right)\right) \tag{2.4}$$

The parameters are defined as follows: ρ represents the density and t denotes time. The velocity components in the $x-$, $y-$, and $z-$directions were given by u, v, and w, respectively. Variable P corresponds to pressure, while v_{eff} represents the effective kinematic viscosity ($v_{eff}=v_t+v$), v_t is the turbulent kinematic viscosity, g is the gravity acceleration (Kheirkhah Gildeh et al., 2015).

2.2.4 Turbulence models

To the best of the authors' knowledge, the current models for vertically confined jets are all based on the Reynolds Averaged Navier-Stokes (RANS) equations, which consider Reynolds averaging to minimize the effects of rapid fluctuations (Savage & Johnson, 2001). In this study, three well-known RANS models were used, namely standard k-*ε*, RNG k-*ε*, and k-*ω* SST.

- Standard k–ε model:

The standard k–ε model is a widely used two-equation turbulence model that calculates the turbulent kinetic energy (k) and its dissipation rate (ε) to simulate the turbulence characteristics. The model assumes that the turbulence is isotropic and homogeneous and is therefore suitable for free shear and wall flows. However, due to the oversimplification of the model, there are limitations in accurately predicting flow separation and return zones (Launder & Spalding, 1974). The equations of the standard k–ε model can be written as (Shaheed et al., 2019).

$$\frac{\partial k}{\partial t}+\frac{\partial k u_i}{\partial x_i}=\frac{\partial}{\partial x_i}\left(Dk_{eff}\frac{\partial k}{\partial x_i}\right)+G_k-\varepsilon \tag{2.5}$$

$$\frac{\partial \varepsilon}{\partial t}+\frac{\partial \varepsilon u_i}{\partial x_i}=\frac{\partial}{\partial x_i}\left(D\varepsilon_{eff}\frac{\partial \varepsilon}{\partial x_i}\right)+C_{1\varepsilon}\frac{\varepsilon}{k}G_k-C_{2\varepsilon}\frac{\varepsilon^2}{k} \tag{2.6}$$

The parameters in the equation can be calculated using the following formula (Shaheed et al., 2019). σ_ε is the turbulent Prandtl number for ε, and is the turbulent Prandtl number, which is set to 1.3.

Dk_{eff} and $D\varepsilon_{eff}$ are the effective diffusivity for k and ε, which can be calculated as:

$$Dk_{eff}=v+v_t \tag{2.7}$$

$$D\varepsilon_{eff}=v+\frac{v_t}{\sigma_\varepsilon} \tag{2.8}$$

v_t is the turbulent kinematic viscosity at each point and is written as:

$$v_t=C_\mu\frac{k^2}{\varepsilon} \tag{2.9}$$

The constants $C_{1\varepsilon}$, $C_{2\varepsilon}$, and C_μ have the following values.

$$C_{1\varepsilon}=1.44,\quad C_{2\varepsilon}=1.92,\quad C_\mu=0.09$$

G_k is the generation of turbulent kinetic energy and is written as:

$$G_k=2v_t S_{ij}^2 \tag{2.11}$$

Where S_{ij} is the strain-rate tensor and is written as:

$$S_{ij}=0.5\left(\frac{\partial u_j}{\partial x_i}+\frac{\partial u_i}{\partial x_j}\right) \tag{2.10}$$

- RNG k–ε model:

The RNG k–ε model is derived using renormalization group (RNG) theory and improves the standard k–ε model by including additional terms in the dissipation rate equation to better handle high strain rate and rapid strain turbulence. The RNG k–ε model improves the accuracy in predicting flow separation and recirculation regions, making it more suitable for complex turbulent flows (Yakhot & Orszag, 1986).

The transport equations of the RNG k–ε model can be expressed as equations 2.11-2.12 (Shaheed et al., 2019).

$$\frac{\partial k}{\partial t}+\frac{\partial k u_i}{\partial x_i}=\frac{\partial}{\partial x_i}\left[\left(x+\frac{v_T}{\sigma_k}\right)\frac{\partial k}{\partial x_i}\right]+G_k-\varepsilon \tag{2.11}$$

$$\frac{\partial \varepsilon}{\partial t}+\frac{\partial \varepsilon x_i}{\partial x_i}=\frac{\partial}{\partial_i}\left[\left(v+\frac{v_T}{\sigma_\varepsilon}\right)\frac{\partial \varepsilon}{\partial x_i}\right]+C_{1\varepsilon}\frac{\varepsilon}{k}G_k-\left(C_{2\varepsilon}+\frac{C_\mu \eta^3\left(1-\frac{\eta}{\eta_0}\right)}{1+\beta\eta^3}\right)\frac{\varepsilon^2}{k} \tag{2.12}$$

- SST k–ω model:

The SST k–ω model is an extension of the standard k–ω model that improves turbulence modeling by combining the k–ω model near the wall with the k–ε model in the free-flow region and incorporating shear stress transport to account for the effects of adverse pressure gradients, making it more suitable for predicting flow separation and boundary layer behavior (Menter, 1993).

The transport equations of the RNG k–ε model can be written as Equations 2.13-2.16 (Lee, 2018).

$$\frac{\partial k}{\partial t}+\nabla\cdot\left(uk\right)=P_k-\beta^* k\omega+\nabla\cdot\left(v+\sigma_k v_t\right)\nabla k \tag{2.13}$$

$$\frac{\partial \omega}{\partial t}+\nabla\cdot\left(u\omega\right)=\alpha D^2-\beta\omega^2+\nabla\cdot\left(v+\sigma_\omega v_t\right)\nabla\omega+2\left(1-F_1\right)\sigma_{\omega 2}\frac{1}{\omega}\nabla k\cdot\nabla\omega \tag{2.14}$$

$$v_t=\min\left(\frac{k}{\omega},\frac{a_1 k}{\Omega F_2}\right) \tag{2.15}$$

$$P_k=\min\left(G,10\beta^* k\omega\right) \tag{2.16}$$

Table 2.2. Coefficients in SST k–ω model (Lee, 2018)

a_1	0.31
β^*	0.09
F_1	$\tanh\left\{\left\{\min\left[\max\left(\frac{\sqrt{k}}{\beta^*\omega y},\frac{500v}{y^2\omega}\right),\frac{4\sigma\omega_2 k}{CD_{k\omega}y^2}\right]\right]\right\}^4\right\}$
F_2	$\tanh\left\{\left[\max\left(\frac{2\sqrt{k}}{\beta^*\omega y},\frac{500v}{y^2\omega}\right)\right]\right]\right\}$
$CD_{k\omega}$	$2\sigma_{\omega 2\frac{1}{\omega}}\nabla k\cdot\nabla\omega$
α	$\alpha_1 F_1 + \alpha_2\left(1-F_1\right) with \alpha_1 = 5/9 and \alpha_2 = 0.44$
β	$\beta_1 F_1 + \beta_2\left(1-F_1\right) with \beta_1 = 3/40 and \beta_2 = 0.0828$
σ_k	$\sigma_{k1}F_1 + \sigma_{k2}\left(1-F_1\right) with \sigma_{k1} = 0.85 and \sigma_{k2} = 1$
σ_ω	$\sigma_{\omega1}F_1 + \sigma_{\omega2}\left(1-F_1\right) with \sigma_{\omega1} = 0.5 and \sigma_{\omega2} = 0.856$

2.2.5 Implementation of the Solver

In this study, simulations were performed using Open Field Operations and Manipulation (OpenFOAM), an open-source Computational Fluid Dynamics (CFD) platform implemented in C++ and widely used in hydraulic engineering applications (Imanian and Mohammadian, 2019). The Finite Volume Method (FVM) is the basis of all OpenFOAM solvers for discretizing and solving the governing equations. The FVM ensures local conservation of mass, momentum, and energy by integrating the equations over a discrete control volume.

To simulate the mixing of two fluids with the same physical properties but different temperatures while capturing the density change due to thermal gradients, a modified solver was developed based on the standard pimpleFoam solver of OpenFOAM. The original solver pimpleFoam is a transient solver designed for incompressible turbulence. It utilizes the PIMPLE algorithm, which combines the Pressure Implicit Splitting of Operators (PISO) method (Issa et al., 1986) with the

Semi-Implicit Method for Pressure Related Equations (SIMPLE). This hybrid algorithm improves the numerical stability and efficiency of simulations involving large time-steps or complex geometries. The flowchart of the PIMPLE algorithm is illustrated in Fig. 2.10. The PIMPLE algorithm is used in the modified solver.

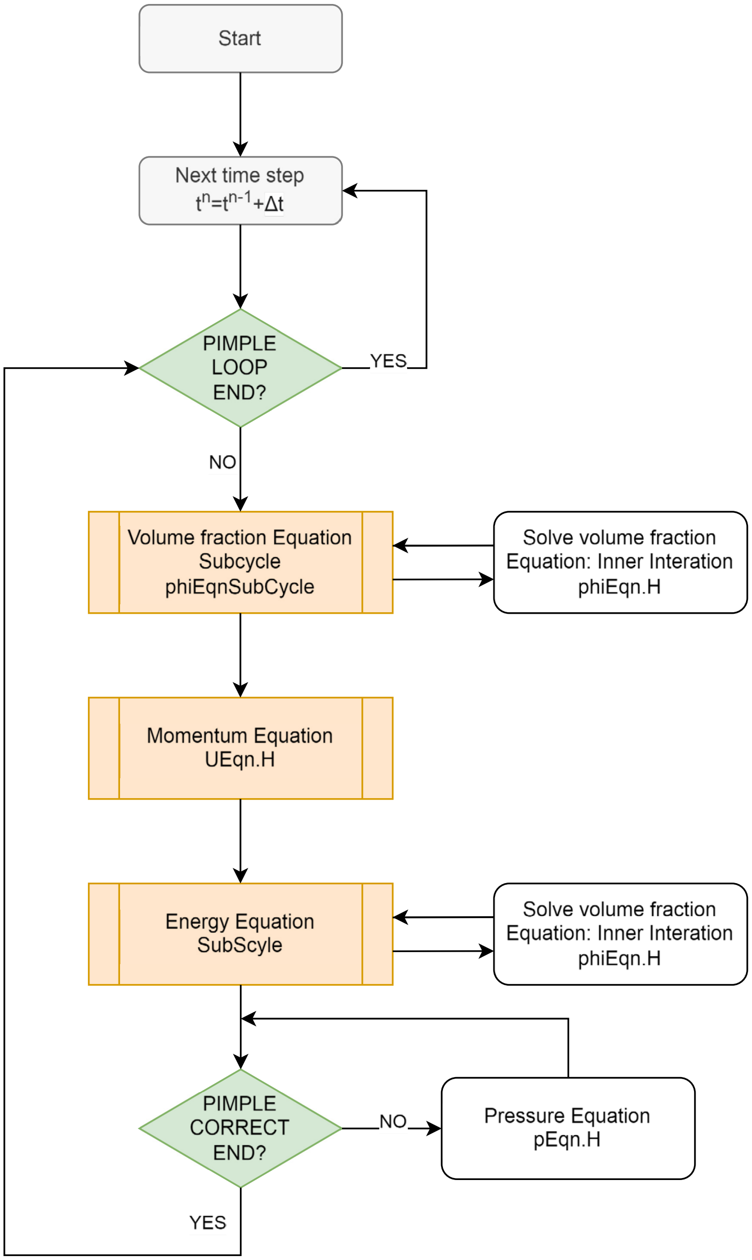

Figure 2.10. PIMPLE algorithm loop flowchart (Amidu et al. 2021)

In this study, a customized solver named pimpleFoam10r was developed by modifying the standard pimpleFoam solver in OpenFOAM. The original solver assumes incompressible flow with constant density, which limits its applicability to buoyancy-driven flows. To overcome this limitation, the solver was extended to include a temperature-dependent density model, enabling the simulation of variable-density flows driven by thermal gradients. Specifically, an energy equation was added for temperature transport, and an additional source term was introduced in the momentum equation to account for buoyancy effects caused by temperature variations. These modifications result in a strong coupling between the energy and momentum equations, allowing the solver to capture thermally induced density variations and their impact on jet behavior.

At each time step, the PIMPLE algorithm performs multiple prediction correction loops to update the velocity, pressure, and temperature fields iteratively. The velocity field is computed implicitly by solving a system of linear equations of the form Ax = b, while the pressure field is updated using Poisson's equation derived from the continuity constraints. The scalar transport equations are solved sequentially using the standard OpenFOAM library to ensure consistent and efficient implementation of thermal coupling.

These enhancements allow the modified solver to simulate thermally driven variable density flows while retaining the computational advantages of the original incompressible formulation. Figure 2.11 illustrates an overview of the solver structure and modifications.

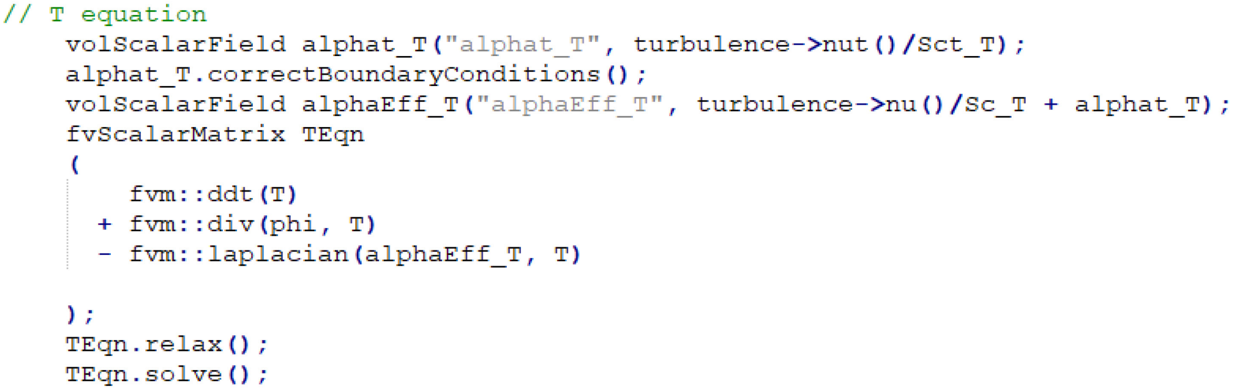

```
// T equation
    volScalarField alphat_T("alphat_T", turbulence->nut()/Sct_T);
    alphat_T.correctBoundaryConditions();
    volScalarField alphaEff_T("alphaEff_T", turbulence->nu()/Sc_T + alphat_T);
    fvScalarMatrix TEqn
    (
        fvm::ddt(T)
      + fvm::div(phi, T)
      - fvm::laplacian(alphaEff_T, T)

    );
    TEqn.relax();
    TEqn.solve();
```

(a)

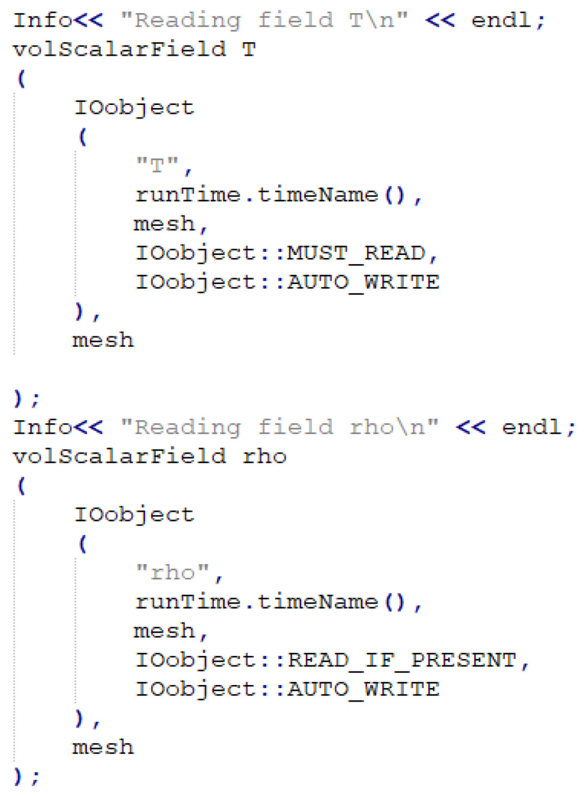

```
Info<< "Reading field T\n" << endl;
volScalarField T
(
    IOobject
    (
        "T",
        runTime.timeName(),
        mesh,
        IOobject::MUST_READ,
        IOobject::AUTO_WRITE
    ),
    mesh

);
Info<< "Reading field rho\n" << endl;
volScalarField rho
(
    IOobject
    (
        "rho",
        runTime.timeName(),
        mesh,
        IOobject::READ_IF_PRESENT,
        IOobject::AUTO_WRITE
    ),
    mesh
);
```

(b)

Figure 2.11. Overview of the solver structure and modifications: (a) Implementation of temperature transfer equations in pimpleFoam10r.C; (b) Definition and initialization of temperature (T) and density (rho) scalar fields in createFields.H

The concentration/temperature equation in openfoam uses the advection-diffusion equation to solve for the concentration/temperature transfer in the system (Kheirkhah Gildeh et al., 2014).

$$\frac{\partial T}{\partial t}+u\frac{\partial T}{\partial x}+\upsilon\frac{\partial T}{\partial y}+w\frac{\partial T}{\partial z}=k_{eff}\left(\frac{\partial^2 T}{\partial x^2}+\frac{\partial^2 T}{\partial y^2}+\frac{\partial^2 T}{\partial z^2}\right) \tag{2.17}$$

With

$$k_{eff}=\frac{\upsilon_t}{\mathrm{Pr}_t}+\frac{\upsilon}{\mathrm{Pr}} \tag{2.18}$$

Where C is the fluid concentration and D is the isotropic diffusion coefficient, T is the fluid temperature, k_{eff} is the heat-transfer coefficient, Pr is the Prandtl number, and Pr_t is the turbulent Prandtl number.

The calculation of density is based on the Millero and Poisson (1981) formula, as shown in equations (2.17-2.18).

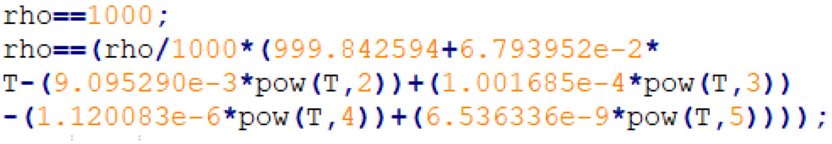

```
rho==1000;
rho==(rho/1000*(999.842594+6.793952e-2*
T-(9.095290e-3*pow(T,2))+(1.001685e-4*pow(T,3))
-(1.120083e-6*pow(T,4))+(6.536336e-9*pow(T,5))));
```

2.2.6 Simulation setup

Figure 2.5a shows a schematic of the simulated experimental tank; which is a wedge-shaped domain, and because the problem is axisymmetric, it is sufficient to select the simulation that considers 5/360 of the tank domain, while the complete outer tank domain is also cylindrical because the selection is angled at the center. The numerical simulation is performed in a cylindrical tank with a radius of 0.25 m and a height of 0.6 m (Fig. 2.12b); a refined grid is used in the simulation, as shown in Fig. 2.12c, to better capture the velocity and concentration in the near-field region, and then the basin inlet at the lower-left end is the densest grid, which gets progressively sparser as the distance gets further away.

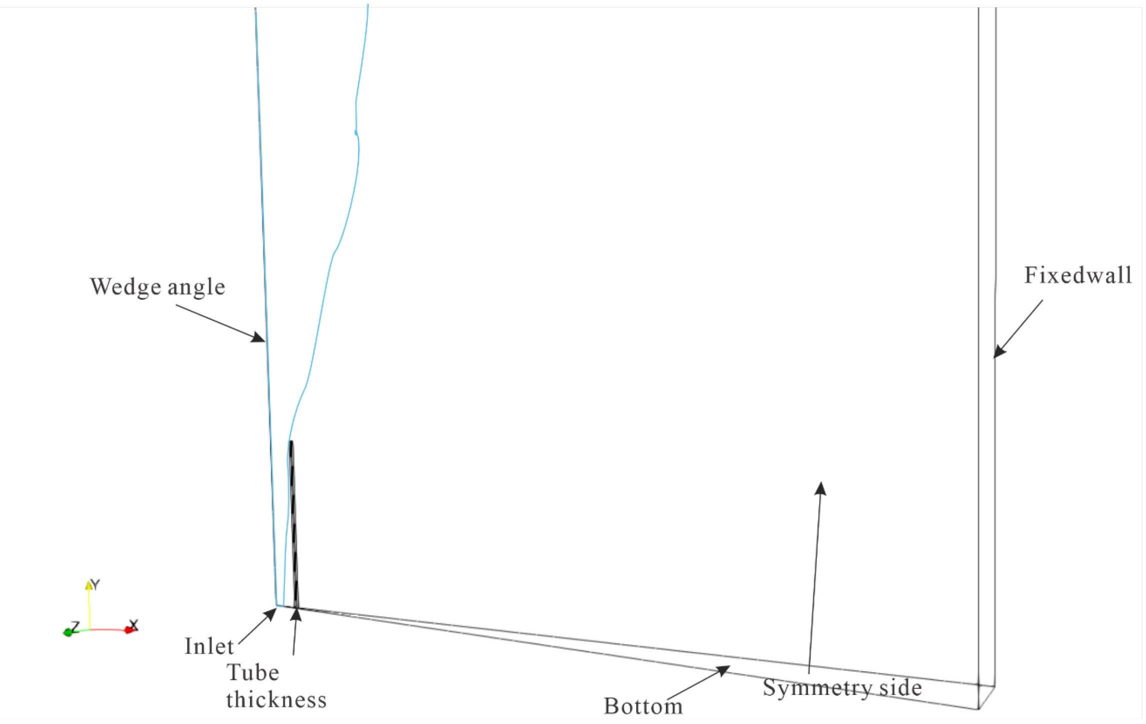

(a)

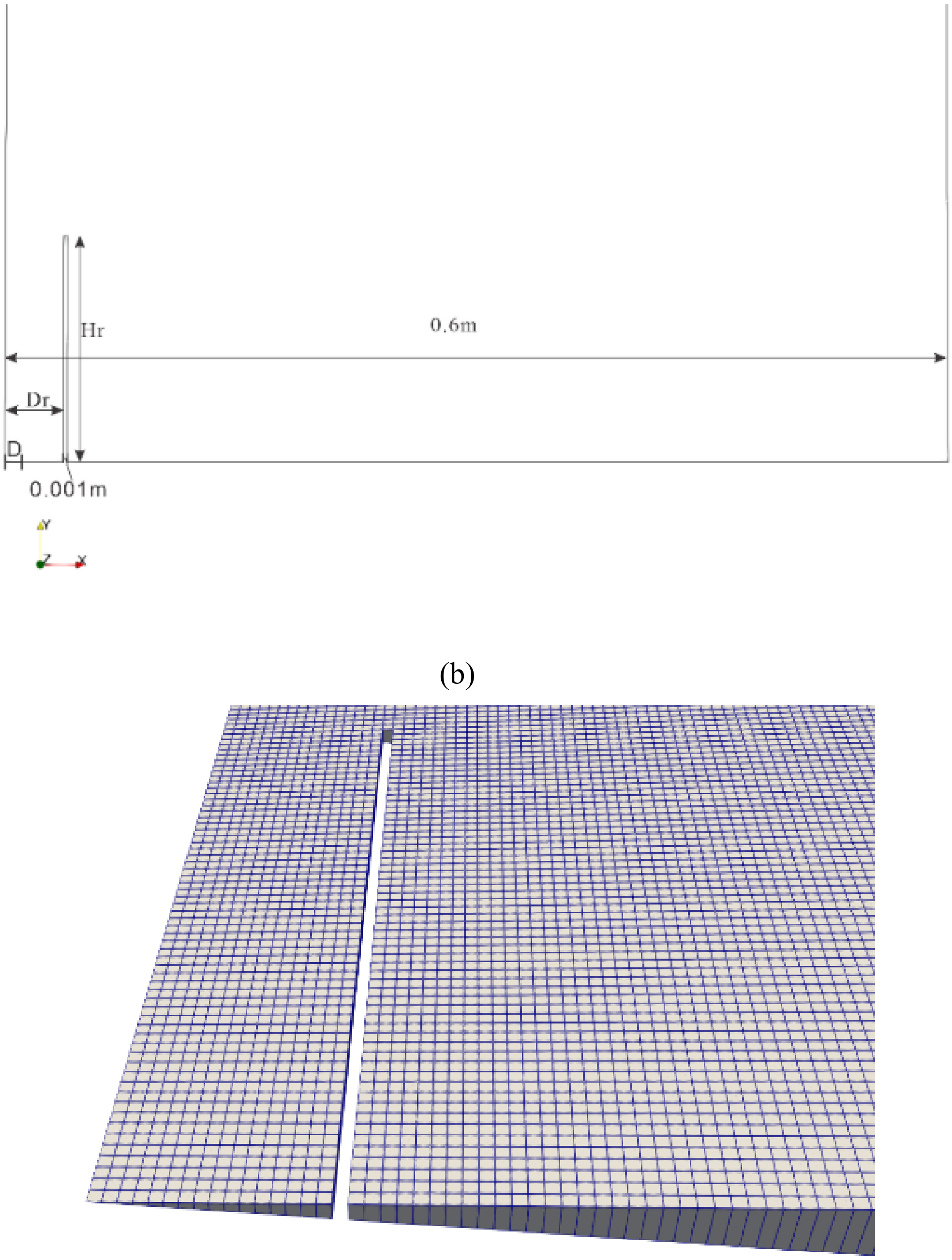

(b)

(c)

Figure 2.12. Schematic diagram of the simulation model (a) 5° axisymmetric wedge-shaped experimental tank; (b) x-y view of the simulation area; (c) grid system of the computational domain.

As in the experiment, the nozzle diameter (D) for the inlet was 6 mm, and the riser diameters were 18 and 31 mm. For the inlet, the boundary conditions are $u = 0$, $v = 0$, $w = U_j$, $T = T0$, $k = 0.006w^2$, $\varepsilon = 0.002w^3/D$, $\omega = \varepsilon/k$, and T = T_j where U is the jet velocity, u v and w are the velocities of the x, y, and z axes, respectively, and k and ε are partially corrected for the different velocities to ensure that the simulation is stable (Kheirkhah Gildeh et al., 2014). In the results and analysis section, S denotes the dilution, which is calculated from C_0/C, where C_0 is the initial concentration and C is the local concentration. T_a represents the temperature, which in this study is 22°C, the same as the ambient water. k is the turbulent kinetic energy and ε is the turbulent kinetic energy dissipation rate. For all walls, the standard wall function was used. In addition, the flow velocities were set to a variety of different velocities according to the settings in Table 2.1. two different riser diameters, two different reiser heights and two different Froude numbers were applied. The surrounding water density was set to 998.1 kg/m^3. For the simulation, the process is shown in Figure 2.13 Flowchart:

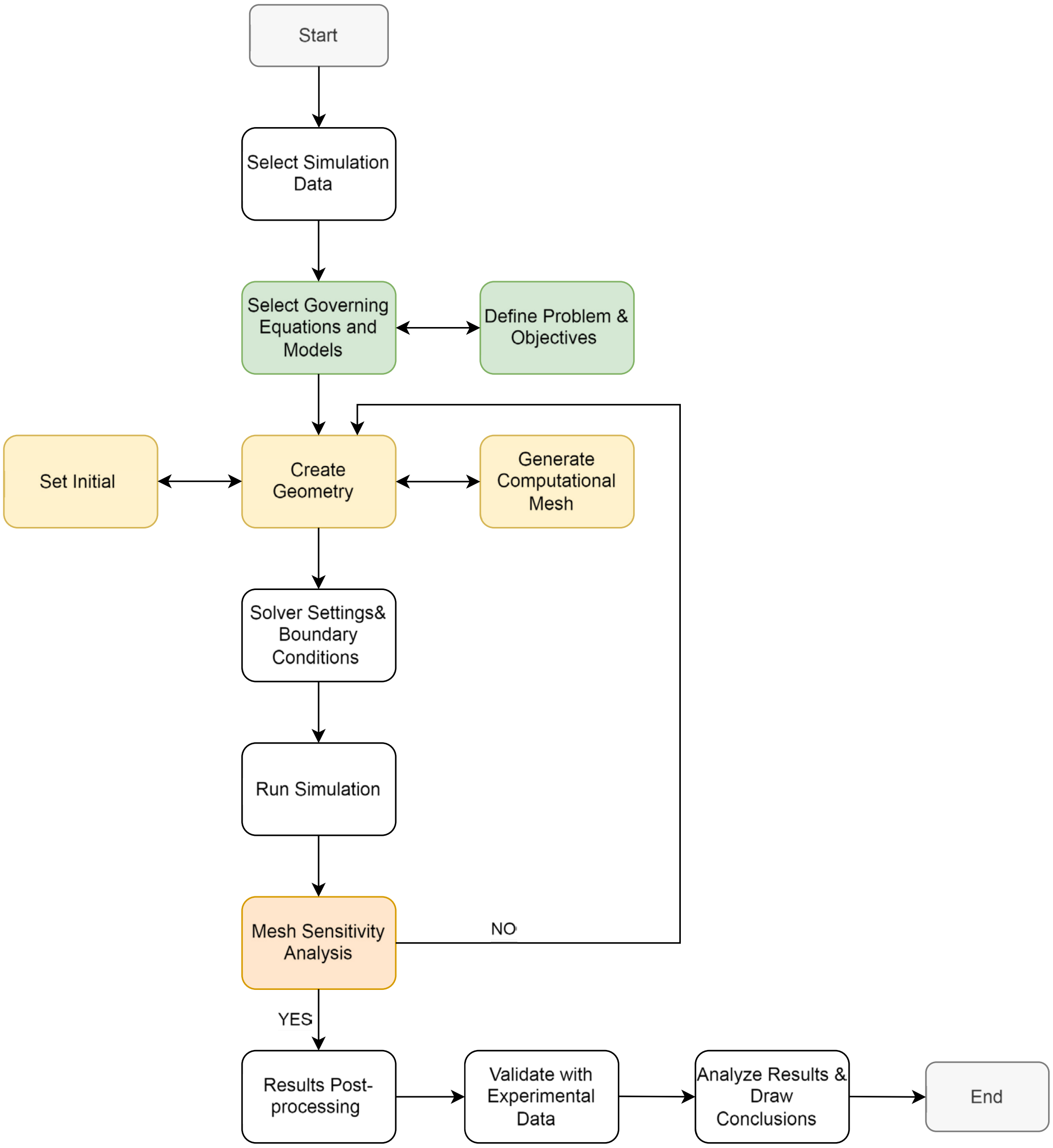

Figure 2.13. Flow of the numerical simulation part.

2.2.7 Convergence and sensitivity tests

In CFD (Computational Fluid Dynamics) simulations, proper meshing not only affects the computational accuracy but is also directly related to the stability and convergence of the computation. In this section, the mesh sensitivity analysis of the simulation results is carried out by setting three different mesh densities: coarse, medium, and fine. Only by ensuring that the grid division is sufficiently detailed and the effects of the more refined grids on the key result variables (e.g., velocity and concentration). tend to converge, it can be shown that the current grid division is sufficiently fine and the simulation results are reliable. Table 2.3 below shows the various coefficients between the three different grids.

Table 2.3. Number of cells and grid quality parameters for different grids

Mesh quantity	Numbers of blocks	Min volume	Max volume	Max aspect ratio	Max skewness
Coarse	120234	4.84×10^{-11}	2.71×10^{-8}	2.24	0.33
Medium	149940	4.35×10^{-11}	2.18×10^{-5}	2.00	0.33
Fine	204374	2.1×10^{-11}	1.6×10^{-8}	2.30	0.33

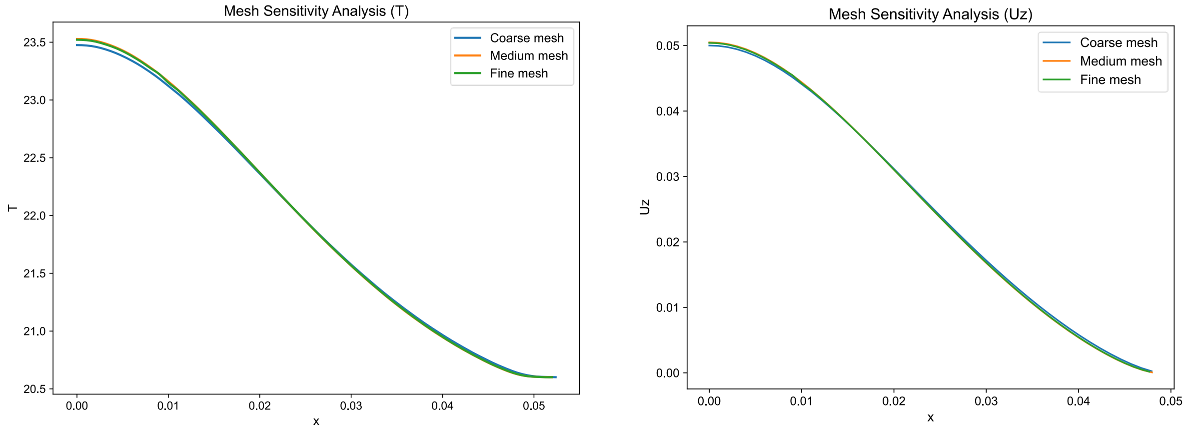

(a) (b)

Figure 2.14. Mesh sensitivity analysis (a) and (b) show the temperature and z-direction velocity distributions in the extended x-direction and z-direction, respectively, for Y/D at 45.

Figure 2.14 shows the effect of mesh quality on the simulation results, with a coarse mesh leading to lower estimates, while the concentration and velocity calculations for the medium and fine meshes are very close to each other. Considering the accuracy, a medium grid was selected for this study.

2.3 Results and discussion

In the experimental section, two different Froude numbers (20, 35), one jet diameter (6 mm), two different riser diameters (18 mm, 31 mm) and two different riser heights (6 mm, 9 mm) were performed.

In the simulation section, two sets of simulations were conducted for two different diameters of risers with different Froude numbers, each of which included three simulations with different turbulence models. Three different diameters and two different heights of risers were included as much as possible in the three sets of simulations, so the total number of simulations conducted was 2 × 3 = 6 sets of simulations. In addition, one additional set of experiments were conducted to demonstrate how the confinement effect affects the flow using the same Fr, Re, and riser height. However, this set of experiment were not validated through simulations. The initial conditions are listed in Table 2.4.

Table 2.4. Case configuration and simulation coverage

Case number	Jet Diameter (mm)	Riser Diameter (mm)	Froude Number	Reynolds number	Riser Height (mm)	Simulation
A1	6	18	20	2358	6	Yes
A2		31	35	3537	9	Yes
C3		18	35	2358	9	No

2.3.1 Experimental Results

Figure 2.15 shows the instantaneous dimensionless concentration field for all test cases, outlining the behavior of the jet under different constraints.

From the comparison of figures 2.15. (a) and (b) and (b) and (c), it can be seen that the confinement effect affects the flow state when the values of Re and Fr are kept constant. Increasing the degree of lateral confinement hinders the cooling process by limiting the interaction of the jet with the ambient fluid.

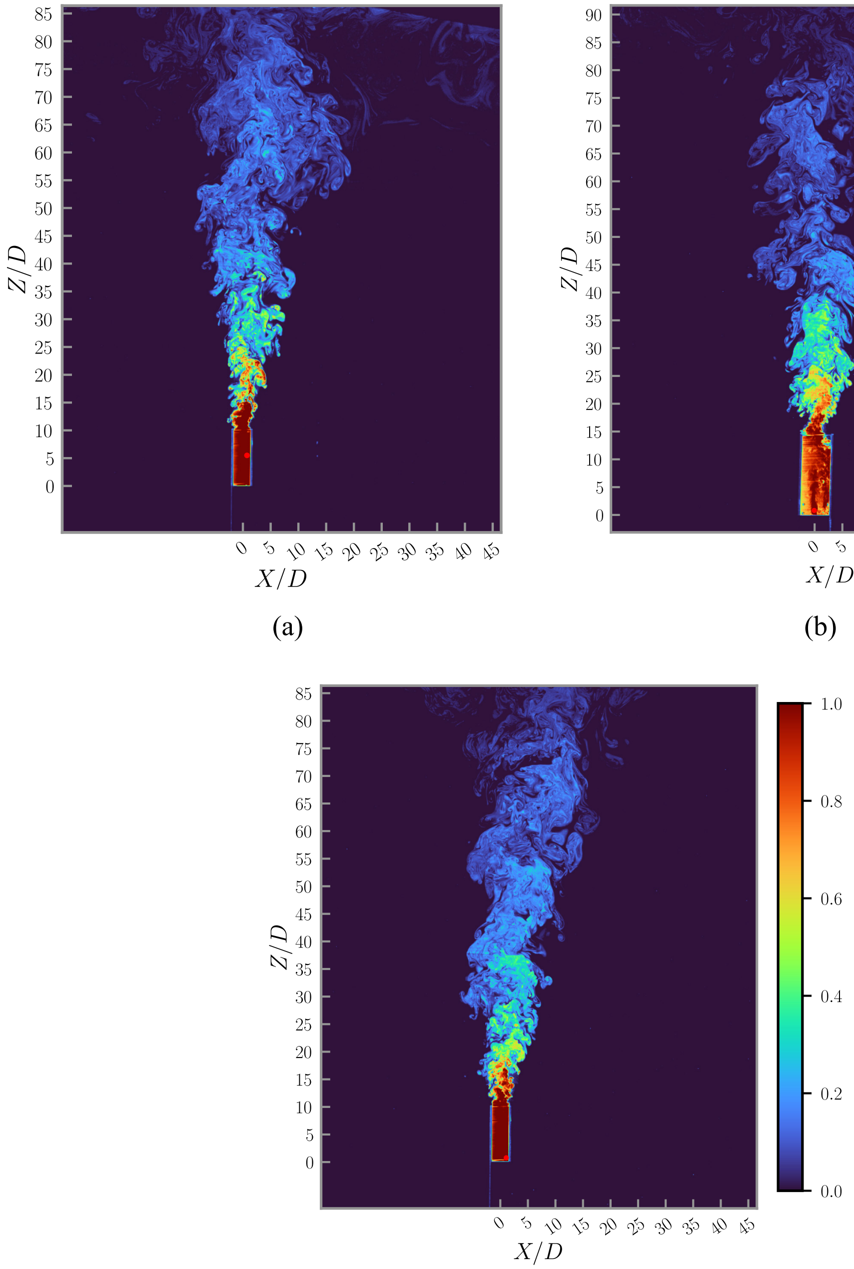

(a)

(b)

(c)

Figure 2.15. Normalized instantaneous concentrations: (a) A1, Fr = 20; (b) A2, Fr = 35; (c) C3, Fr = 35.

Because the primary objective of this study was to investigate the time-averaged behavior of a vertically constrained buoyant jet, the analysis focused on the mean concentration field rather than the instantaneous flow structure. Although instantaneous LIF images provide relevant images of jet transients and turbulence features, they exhibit significant temporal fluctuations. Therefore, to obtain reproducible data for the next step of validation and OpenFOAM modeling, the focus was placed on the statistical mean of the concentration field, which better represents the steady-state characteristics of jet dilution and mixing. The effects of random fluctuations and noise can be minimized by averaging 3000 image frames in Figure 2.16, allowing a clearer assessment of the centerline dilution trend. This approach is consistent with the overall goal of comparing experimental observations with CFD simulations based on RANS, which predict the time-averaged flow behavior.

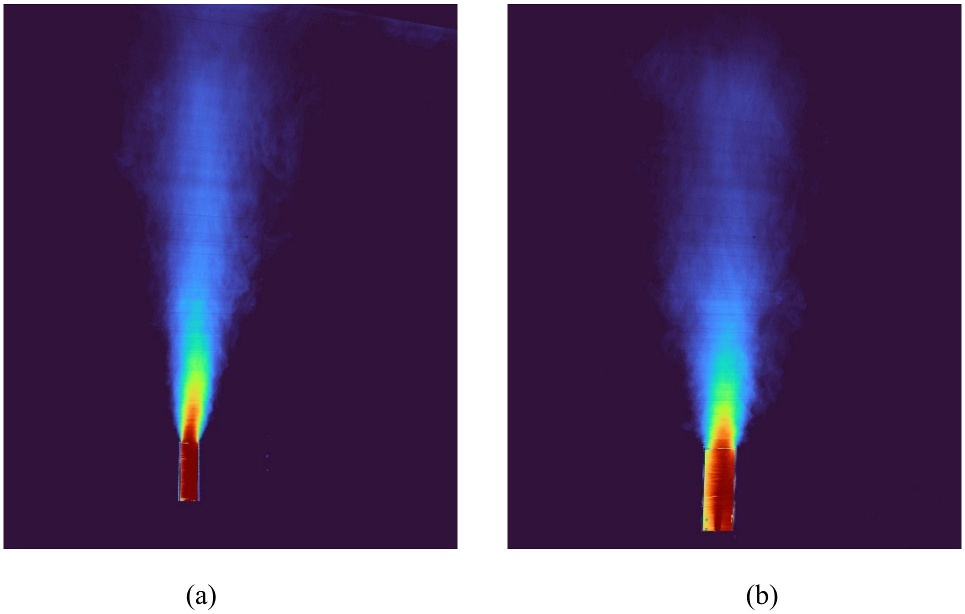

(a) (b)

Figure 2.16. Normalized time-averaged concentrations: (a) A1, Fr = 20; (b) A2, Fr = 35.

2.3.2 Simulation Results

Before a detailed comparison with the experimental data can be made, the reasonableness of the simulation results must be verified. Figure 2.17 shows the temperature fields obtained from the numerical simulations for the two selected experimental cases (A1 and A2). For each case, we simulated three RANS turbulence models: standard k–ε, RNG k–ε, and SST k–ω.

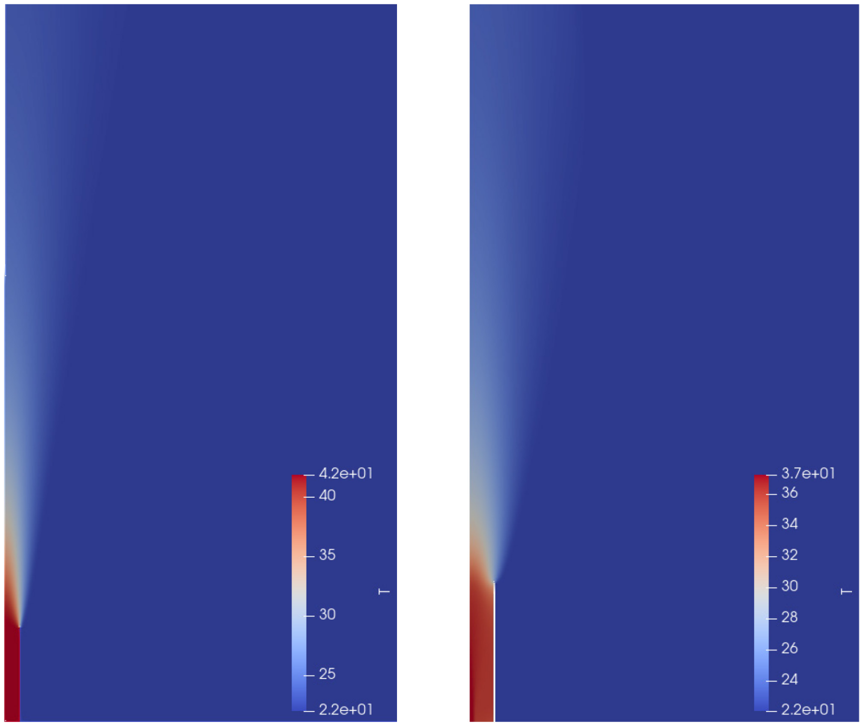

(a) (b)

Figure 2.17. Simulated concentration results: (a) A1, Fr = 20; (b) A2, Fr = 35.

The vertical development of the buoyant jet can be clearly observed in these images. The jet rose from the nozzle and forms a distinctly higher temperatur core along the centerline. As the jet rises, it spreads laterally due to the entrainment of the surrounding fluid, resulting in a gradual decrease in the temperature away from the jet axis with increasing vertical distance. The shape and extent of the temperature profile vary across the two flow conditions, reflecting the effects of the buoyancy strength and lateral confinement.

2.3.3 Centerline Maximum Concentration

To evaluate the predictive performance of the turbulence models, the centerline concentration profiles of the experimental measurements and numerical simulations for cases A1, A2 were compared. The experimental concentration profiles were obtained from the time-averaged LIF images by extracting the intensity values along the jet centerline, whereas the simulated concentration data were extracted directly from the OpenFOAM calculation results.

The focus of this comparison is the centerline vertical decay of the concentration as the buoyant jet rises, which is a key indicator of the mixing and entrainment behavior. In particular, the centerline highest concentration (C) is used as a representative metric for assessing the retained scalar content along the jet axis. To enable meaningful comparison across different cases, all concentration values were normalized using the inlet jet concentration C_0 as the reference. The normalized concentration $\widehat{C}$ is defined as:

$$\widehat{C} = \frac{C}{C_0} \tag{2.19}$$

where C is the local concentration at a given location, and C_0 is the concentration measured at the jet exit. This normalization ensures consistency in evaluating the decay behavior regardless of differences in flow configuration or input strength.

The focus of this comparison is the centerline vertical decay of the concentration as the buoyant jet rises, which is a key indicator of the mixing and entrainment behavior. Figure 2.18 shows the concentration curves for each case, showing the experimental data and predictions of the standard k–ε, RNG k–ε, and SST k–ω turbulence models. The absolute values of the concentrations were not normalized but were taken directly from the experimentally captured data, and consistent reference points were used for both the experimental and numerical datasets to enable direct and accurate comparison of the curve shapes and decay rates.

To quantify the level of agreement between the simulations and experiments, three statistical metrics were used: squared Pearson correlation coefficient (R^2), normalized root mean square error (NRMSE), and mean absolute error (MAE). This was performed to evaluate the correlation and deviation between the simulated and experimental centerline concentration profiles.

The statistical metrics used in this study are defined as follows:

$$R^2 = 1 - \frac{\sum_{i=1}^{n}\left(y_i - \hat{y}_i\right)^2}{\sum_{i=1}^{n}\left(y_i - \overline{y}\right)^2} \tag{2.20}$$

$$NRMSE = \frac{\sqrt{\frac{1}{n}\sum_{i=1}^{n}\left(y_i - \hat{y}_i\right)^2}}{y_{\max} - y_{\min}} \tag{2.21}$$

$$MAE = \frac{1}{n}\sum_{i=1}^{n}\left| y_i - \hat{y}_i \right| \tag{2.22}$$

where $\hat{y}_i$ is the simulated value, y_i is the corresponding experimental value, $\overline{y}$ is the mean of the experimental values, $y_{\max}$ and $y_{\min}$ are the maximum and minimum observed values, and nnn is the total number of data points. The results are summarized in Table 2.5.

Table 2.5. Statistical evaluation of centerline concentration predictions for each turbulence model and case.

Case	Turbulence Model	R²	NRMSE	MAE
A1	standard k-ε	0.9956	0.0270	0.0200
	RNG k-ε	0.9929	0.0368	0.0256
	SST k-ω	0.9576	0.0928	0.0625
A2	standard k-ε	0.9953	0.0603	0.0533
	RNG k-ε	0.9776	0.0614	0.0394
	SST k-ω	0.8820	0.1721	0.1205

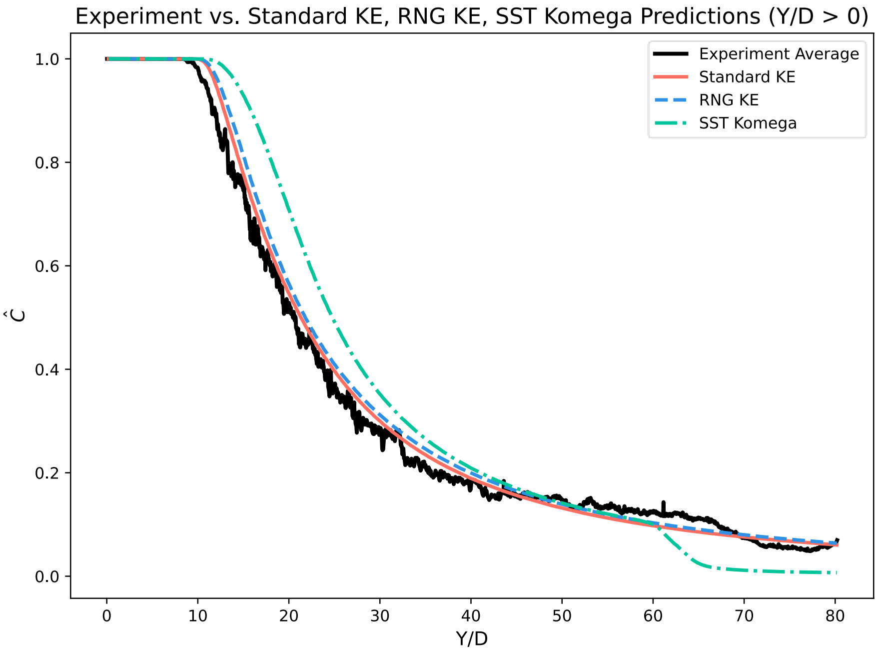

(a)

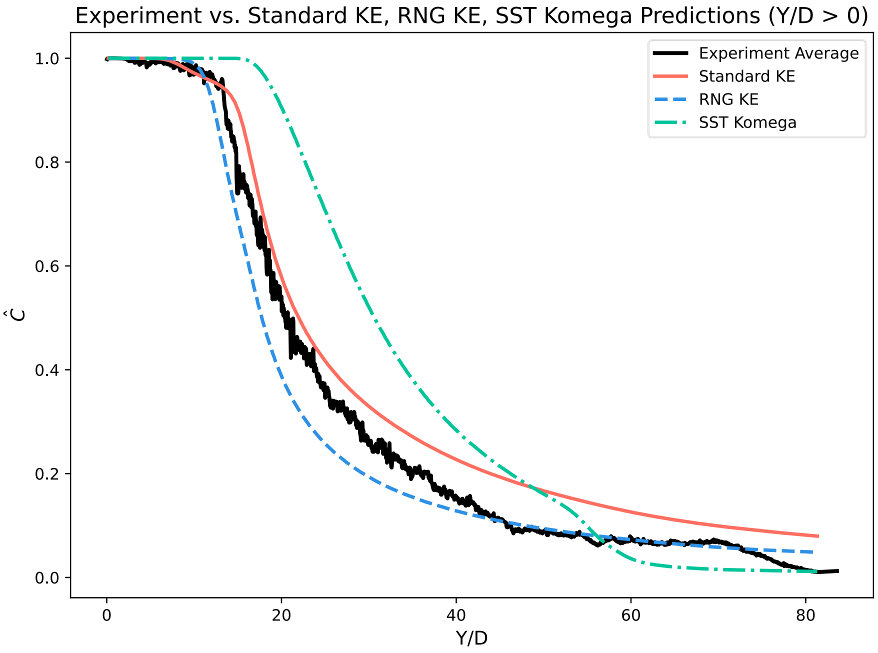

(b)

Figure 2.18. Comparison of experimental and simulated centerline concentration distributions using standard k-ε, RNG k-ε, and SST k-ω turbulence models. (a) Case A1; (b) Case A2.

As can be seen from the statistical metrics in Figure 2.18 and Table 2.5, the standard k-ε model is in the best overall agreement with the experimental data in Cases A1 and A2, followed by the RNG k-ε model, the SST k–ω model has a higher value of concentration on the centerline of the prediction in the early stage and then decreases rapidly in the later stage, which is even lower than the experimental one, resulting in a slightly lower R^2 and a higher value of the error, however, its performance remains acceptable in both cases. Meanwhile, all three models yield relatively low NRMSE values, indicating that the overall magnitude of prediction errors is within an acceptable range and supports the reliability of the numerical predictions.

2.3.4 Lateral Concentration Comparison

To further evaluate the accuracy of the turbulence model in predicting the lateral mixing behavior of vertically confined buoyant jets, lateral concentration profiles were extracted at two representative vertical locations: Y/D = 20 and Y/D = 45, which correspond to different stages of jet development, with Y/D = 20 representing the near-field region near the nozzle outlet and Y/D = 45 located in the mid to far field, where stronger dilution and lateral diffusion have already occurred.

The lateral profile data for the experiment were obtained by sampling the horizontal line on the time-averaged LIF image at the specified Y/D position. The corresponding numerical profiles were extracted from the OpenFOAM simulation results using horizontal slices at the same locations. The comparison results include those from the standard k–ε, RNG k–ε, and SST k–ω turbulence models.

As the jet is symmetric about the vertical centerline, the left and right sides of the jet are expected to exhibit mirror symmetry for a given flow condition, with only the right half of the lateral concentration distribution shown in the figure. All profiles were plotted relative to the jet axis, with the horizontal coordinates indicating the normalized lateral distance from the centerline. Figure 2.19 shows the lateral concentration distributions at Y/D = 20 and Y/D = 45.

To quantitatively assess the agreement between the simulations and experiments, the Pearson coefficient of correlation (R^2) and normalized root mean square error(NRMSE) was calculated for each case at both sampling heights, and the results are summarized in Table 2.6.

Table 2.6. Performance metrics (Pearson R^2 and NRMSE) for lateral concentration profiles at Y/D = 20 and Y/D = 45 for different cases and turbulence models.

Case	Y/D	Metric	Standard k–ε	RNG k–ε	SST k–ω
A1	20	R^2	0.947	0.947	0.891
		NRMSE	0.1060	0.1125	0.2228
	45	R^2	0.982	0.983	0.980
		NRMSE	0.0632	0.0986	0.1136
A2	20	R^2	0.989	0.976	0.915
		NRMSE	0.1056	0.1674	0.4825
	45	R^2	0.883	0.966	0.847
		NRMSE	0.3891	0.0621	0.4621

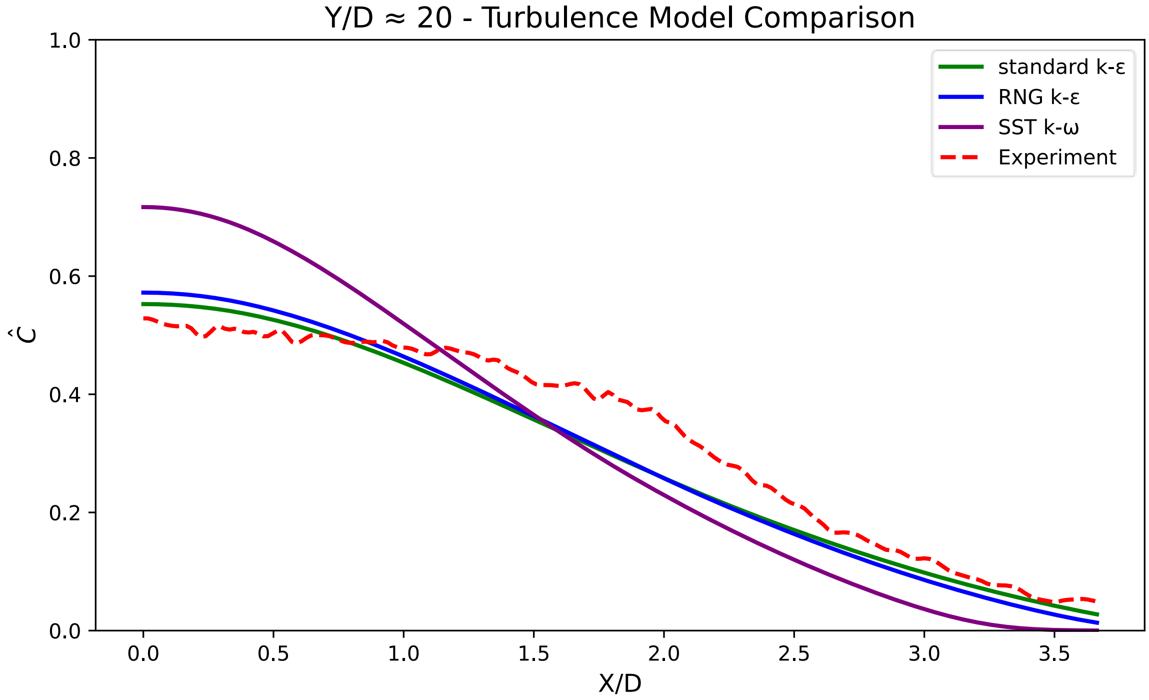
Y/D ≈ 20 - Turbulence Model Comparison
1.0
0.8
0.6
0.4
0.2
0.0
$\hat{C}$
0.0
0.5
1.0
1.5
2.0
2.5
3.0
3.5
X/D
standard k-ε
RNG k-ε
SST k-ω
Experiment

(a)

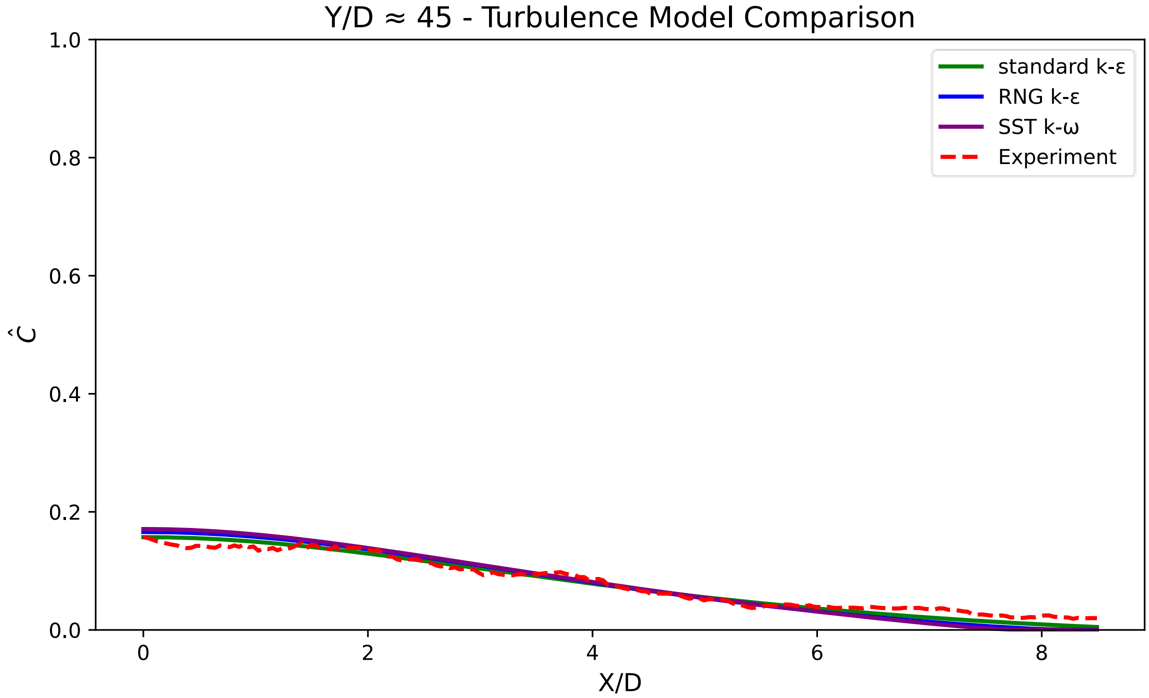
Y/D ≈ 45 - Turbulence Model Comparison
1.0
0.8
0.6
0.4
0.2
0.0
$\hat{C}$
0
2
4
6
8
X/D
standard k-ε
RNG k-ε
SST k-ω
Experiment

(b)

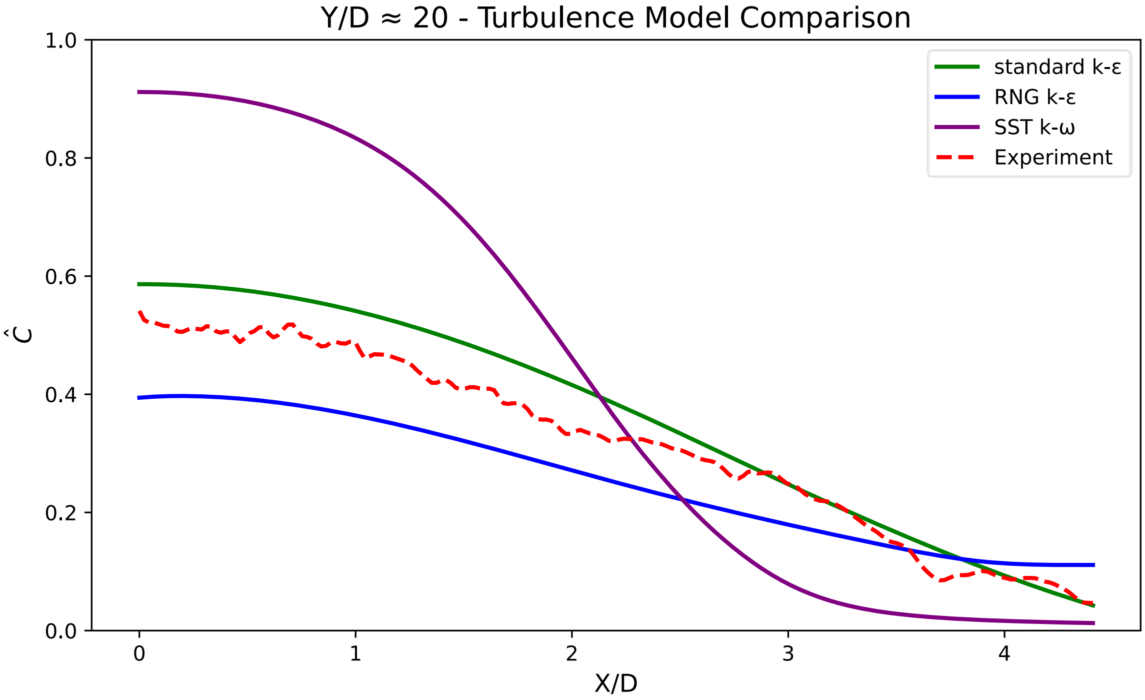

(c)

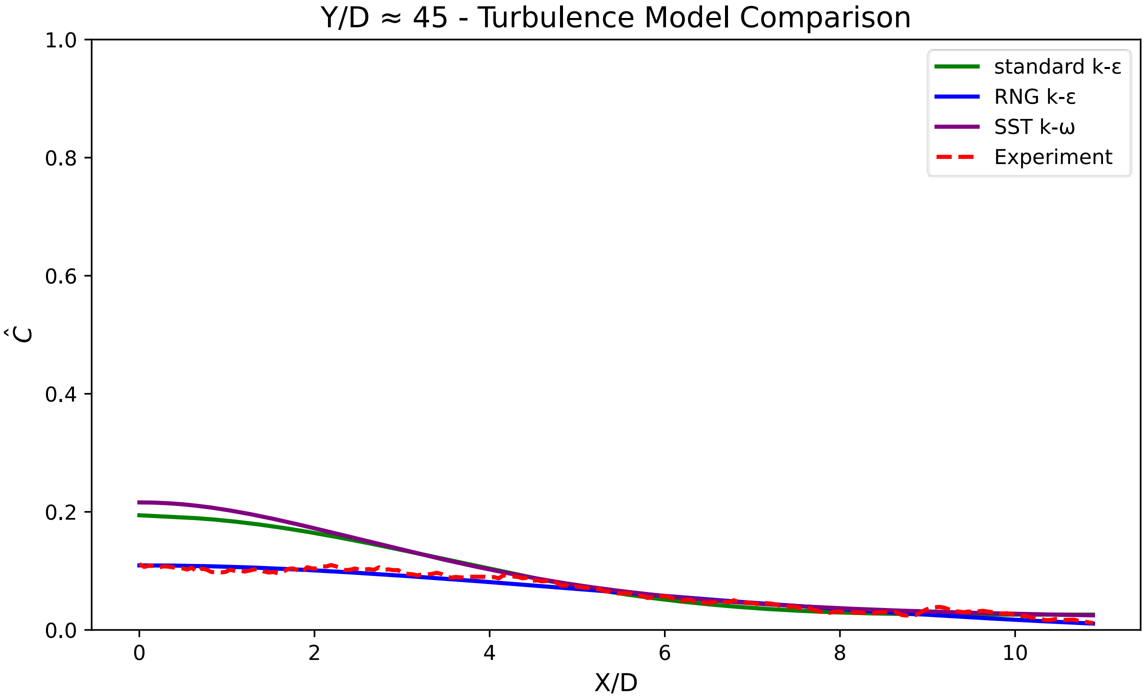

(d)

Figure 2.19. Lateral concentration profiles at Y/D = 20 and Y/D = 45 for Cases A1–A2. (a) A1, Y/D = 20 (b) A1, Y/D = 45 (c) A2, Y/D = 20 (d) A2, Y/D = 45

The accuracy of the turbulence models in predicting the lateral concentration distribution varies significantly between the three cases and different vertical positions, as shown in Figure 2.19 and Table 2.6. For case A1, all models show reasonable agreement with the experimental data. Both the standard and RNG k-ε models achieve high R^2 and NRMSE values at Y/D = 20 and 45, while the SST k-ω model is quite accurate at Y/D = 45, although slightly less accurate at Y/D = 20. In contrast, Case A2 shows a large difference between the models, with the SST k–ω model performing poorly at both heights. The standard k–ε model shows moderate agreement at Y/D = 20 but performs poorly at Y/D = 45, NRMSE value is a little high relative to other turbulence models and value in case A1 while the RNG k-ε model captures the far-field distribution at Y/D = 45 with high accuracy. The overall comparison shows that the standard k-ε model, although less accurate in one case, is better overall.

2.3.5 Discussion

The squared Pearson correlation coefficient (R^2) is a widely used metric for assessing the agreement between predicted and measured trends, but it primarily reflects the consistency of the overall shape rather than the absolute accuracy of the predicted values. Thus, a model can obtain a high R^2 even if the predicted values deviate significantly from the measured values. To address this limitation, in chapter 2.3.3 and 2.3.4, we also use the normalized root mean square error (NRMSE) as it takes into account both the magnitude and distribution of the prediction error. By combining R^2 and NRMSE, a more comprehensive assessment of model performance can be made while capturing trend adjustment and numerical accuracy.

To strengthen the proof and to exclude chance, Experiment C3 was simulated again with the same diameter as A1 and the same height and temperature as A2, and the agreement of the experimental concentration profiles with the simulated concentration profiles in Case C3 was comparable to those in Cases A1 and A2. This agreement is further evidence that these models are able to accurately reproduce the centerline dilution behavior in the laterally confined buoyant jet scenario.

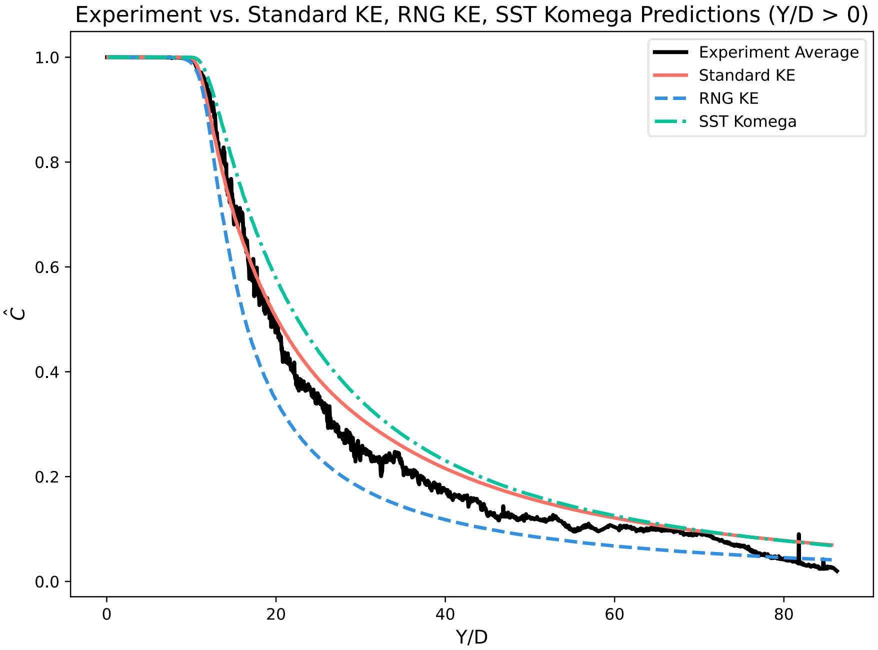

Figure 2.20. Comparison of experimental and simulated centerline concentration distributions for Case C3 using standard *k–ε*, RNG *k–ε*, and SST *k–ω* turbulence models.

Figure 2.20 illustrates the comparison of the experimental concentration profiles with the simulated concentration profiles in Case C3 using the standard k-ε, RNG k-ε, and SST k-ω turbulence models. All three models show very good agreement with the experimental data. Specifically, the standard k-ε model achieves an R^2 value of 0.9967, which indicates an excellent prediction accuracy, while the RNG k-ε and SST k-ω models also perform well with R^2 values of 0.9829 and 0.9894, respectively.

These results confirm that all three turbulence models are reliable for predicting the mixing characteristics of confined buoyant jets. The high degree of agreement observed in C3 and the results of A1 and A2 enhance the robustness and accuracy of these models in different constrained configurations, further validating their applicability for simulation-based analysis in similar engineering environments.

2.4 conclusion

In this chapter, a comprehensive study of vertically constrained buoyant jets was presented using laboratory experiments and CFD simulations. The experimental setup based on the LIF technique successfully captured the detailed concentration fields under multiple constraint configurations. Corresponding numerical simulations were performed using OpenFOAM, and several RANS turbulence models (including the standard k–ε, RNG k–ε, and SST k–ω) were used to evaluate the performance of the models under various jet conditions.

A comparison of the experimental and simulated centerline concentrations revealed that the standard k–ε model generally provided the most consistent and accurate predictions, with R^2 values in some cases exceeding 0.99. The RNG k–ε and SST k–ω models also showed reasonable accuracy but varied considerably depending on the situation and vertical position.

These observations were further confirmed by lateral concentration profiles at Y/D = 20 and 45. The standard and RNG k–ε models showed strong agreement in the highly constrained configurations, while the SST model produced inconsistent results, especially in Case A2. To further assess the reliability of the models, another test case with strong confinement (18 mm) was simulated (Case C3). A comparison of the centerline concentrations in this case showed that all three turbulence models were in very good agreement. In particular, the R^2 of the standard k–ε model exceeded 0.99, and the corresponding NRMSE values across all models remained low, indicating that the predicted concentration magnitudes were also in close agreement with the experimental data.

The next chapter explores the application of machine learning techniques to further improve prediction accuracy and computational efficiency.

Chapter 3 Application of machine learning in simulation of vertical confined buoyant jet

3.1 Introduction and literature review

3.1.1 Introduction

Wastewater discharge management has become a growing environmental problem in recent decades, especially in coastal and urban riverine environments. Industrialization, urbanization, and population growth have significantly increased the amount of wastewater discharged into natural water bodies (Schewe, Jacob, et al., 2014). Buoyant jets represent a common and complex phenomenon among the various discharges. The density of wastewater is lower than that of ambient water due to its elevated temperature or the presence of lighter dissolved substances. As the incident stream is injected into the ambient water system, the wastewater rises due to buoyancy and momentum, spreading horizontally at the water surface. The behavior of these jets is influenced by several factors, including initial velocity, density differences, ambient water flow, and stratification (Jones, Gilbert R., et al., 2007; Zhang, Shuai, et al., 2016).

Confined jets are a common feature of various wastewater discharge terminals, attracting extensive research interest due to their complex flow dynamics and practical applications (Yan and Mohammadian, 2017). This approach ensures that the pollutants are more evenly distributed and diluted, reducing their environmental impact. The controlled nature of confined jets allows for better management of flow dynamics, including the initial velocity, direction, and turbulence, which are essential for effective wastewater treatment. Numerous studies have provided valuable data on local concentration distribution, inlet velocity profiles, and static pressure variations. In addition, vertical variations in centerline dilution can be easily observed using the laser-induced fluorescence (LIF) experimental technique, resulting in a comprehensive dataset on laterally confined buoyant jets (Lee and Lee, 1998; Shinneeb, A. M., et al., 2011). This extensive data collection has also allowed a detailed assessment of the impacts of wastewater discharge and dispersion processes on ambient waters.

Despite the advancements in buoyant jet modeling, there are very limited studies specifically focused on the use of AI for predicting the dynamics of laterally confined vertical buoyant jets. Notably, Yan and Mohammadian (2019) introduced a novel approach for predicting the initial dilution of these jets using multigene genetic programming (MGGP) techniques. Their research highlighted the superior performance of the MGGP-based model compared to single gene genetic programming (SGGP) models and existing regression-based empirical equations. Zhao et al. (2022) have demonstrated that ANFIS can achieve high prediction accuracies and outperform traditional empirical and MGGP methods, thus confirming its potential as a reliable modeling tool for such flow configurations. While these studies represent a significant step forward, systematic AI-driven predictions for vertical confined buoyant jets remain lacking. However, AI techniques have gradually been applied across various scientific and engineering fields, consistently demonstrating strong predictive capabilities. Building upon this momentum, this study seeks to bridge the gap by integrating three prominent data-driven AI models, Adaptive Neuro-Fuzzy Inference System (ANFIS), Extreme Learning Machine (ELM), and Multivariate Adaptive Regression Spline (MARS), to predict the vertical centerline dilution in a laterally confined buoyant jet. The objective is to evaluate and compare their performance, identify the most suitable methods for enhancing prediction accuracy, and ultimately improve the design of environmentally sustainable wastewater discharge systems.

3.1.2 Literature Review

Simulating vertical confined buoyant jets, which involve complex fluid dynamics such as flow rates, density differences, and mixing, can significantly benefit from the application of machine learning algorithms. These jets are characterized by highly nonlinear interactions between key parameters, including the flow rate, density differences, and confinement geometry, which collectively influence the behavior of the jet in terms of velocity profiles, mixing rates, and spread angles.

Traditional simulation methods, like Computational Fluid Dynamics (CFD), are computationally intensive and time-consuming, especially when dealing with large datasets or real-time applications. Machine learning offers a promising data-driven approach that can accelerate predictions and enhance simulation efficiency by learning from historical data and identifying complex patterns without the need for explicit physical modeling. This makes ML particularly attractive for simulating buoyant jet behavior, where interactions among parameters are often too complex for conventional methods.

For this study, three machine learning algorithms, ANFIS, MARS, and ELM. were selected. These algorithms are known for their strong capabilities in regression analysis and nonlinear modeling, which are crucial for capturing the complex dynamics of buoyant jets. However, their application to buoyant jet simulations is still an emerging area, and their effectiveness must be carefully evaluated to ensure they can provide reliable and accurate predictions under various operating conditions.

Adaptive Neuro-Fuzzy Inference System (ANFIS), introduced by Jang (1993), integrates neural network learning capabilities with the interpretability and structured reasoning provided by fuzzy logic systems. Utilizing a hybrid learning algorithm combining gradient descent and least squares estimation (LSE), ANFIS effectively optimizes fuzzy inference parameters, making it highly suitable for modeling complex, nonlinear, and uncertain systems across a wide range of applications such as system identification, prediction, and control tasks.

Recent studies have further validated ANFIS's broad applicability and effectiveness. Jasmine et al. (2022) applied ANFIS to estimate evaporation rates in an arid region of the United States, demonstrating superior predictive accuracy and computational simplicity compared to hybrid ANFIS models combined with optimization algorithms like Firefly Algorithm (FFA), Genetic Algorithm (GA), and Particle Swarm Optimization (PSO). Similarly, Zhao et al. (2022) employed ANFIS to predict dilution patterns of vertically confined buoyant jets using dimensionless parameters (Fr, β, Y/D), achieving a significant reduction in prediction errors compared to empirical equations and multigene genetic programming (MGGP).

Moreover, studies by Dastgheib et al. (2013) and Hipni et al. (2013) underscored ANFIS's effectiveness in hydraulic and hydrological forecasting applications. Dastgheib et al. demonstrated ANFIS's capability to predict the hydraulic properties and trajectory boundaries of circular buoyant jets more accurately than artificial neural networks (ANN). Meanwhile, Hipni et al. highlighted its superior predictive ability in forecasting daily water levels at the Klang Gate Dam, outperforming support vector machine (SVM) models. Collectively, these investigations reinforce ANFIS's robustness, accuracy, and versatility, establishing it as a reliable and powerful modeling tool in environmental hydraulics, water resource management, and related f orecasting disciplines.

Extreme Learning Machine (ELM), proposed by Huang et al. (2006), is a single-hidden-layer feedforward neural network known for its fast training speed and strong generalization performance. Unlike traditional neural networks that rely on iterative optimization, ELM randomly assigns input weights and biases and determines output weights through least squares resolution, substantially reducing computation time and avoiding local minima issues. Owing to these characteristics, ELM has been increasingly adopted for complex nonlinear system modeling tasks.

Recent studies have demonstrated the effectiveness of ELM across various water-related applications. Ebtehaj et al. (2018) developed an integrated ELM framework to predict local scour depths around pile complexes under clear water conditions. By incorporating variables such as flow properties, pile geometry, and sediment characteristics, the ELM model captured complex nonlinear interactions with high accuracy, outperforming traditional machine learning models like support vector machines (SVMs) and artificial neural networks (ANNs), and achieving $R^2 = 0.99$ with a RMSE of 0.007.

In water demand forecasting, Li et al. (2024) proposed a hybrid modeling approach that integrated socio-economic and climatic factors with an ELM optimized by an improved ant colony nesting algorithm (IANA). Their model achieved high predictive accuracy for key drivers such as population growth and rainfall, significantly outperforming multiple benchmark optimization techniques and showcasing ELM's adaptability to dynamic input conditions. Similarly, Anmala and Turuganti (2021) evaluated ELM against various decision tree algorithms for predicting river water quality parameters including fecal coliform, turbidity, pH, and conductivity in the Upper Green River Watershed. Although Random Forest (RF) models exhibited superior overall performance, ELM models demonstrated competitive predictive capabilities with substantially reduced computational time, highlighting their suitability for real-time water quality monitoring applications.

In infrastructure management, Sattar et al. (2019) utilized an ELM model to predict watermain failure times based on a dataset comprising over 9,500 instances from the Greater Toronto Area. By integrating pipe attributes such as length, diameter, material, protective measures, and historical failure data, the ELM model outperformed conventional ANN and SVM approaches, providing a valuable decision-support tool for proactive maintenance and rehabilitation planning.

Multivariate Adaptive Regression Spline (MARS), first introduced by Friedman (1991), is a powerful nonparametric regression method designed to capture complex nonlinear relationships and interactions among variables.MARS constructs models by fitting segmented linear regressions, automatically selecting the variables of interest, and determining the optimal breakpoints and interaction terms without the need for predefined functional forms. Its interpretability and ability to handle high-dimensional nonlinear data have led to a wide range of applications in a variety of research areas such as environmental modeling, econometrics, and bioinformatics.

For water quality studies, Kisi and Parmar (2016) used MARS to predict the monthly chemical oxygen deman of the Yamuna River in India. Their results showed that the performance of MARS was comparable to the Least Square Support Vector Machine (LSSVM) and significantly better than the M5 model tree, especially in predicting high COD concentrations. In addition, Jumber et al. (2024) combined MARS with the Weighted Arithmetic Water Quality Index (WAWQI) method for drinking water quality assessment. Of the nine machine learning models evaluated, MARS had the highest predictive performance, achieving RMSE = 0.090 and $R^2 = 0.87$ on the test dataset, outperforming other methods such as Random Forest, Support Vector Machines, and Artificial Neural Networks.

Recent studies further illustrate the versatility and robustness of MARS.Nayeem et al. (2024) successfully applied MARS to analyze the coloration process during lactose electroactivation in food engineering. Their study, which incorporated variables such as reaction type, reaction time, and CIE Lab* color parameters, demonstrated the effectiveness of MARS in capturing nonlinear relationships and identifying key factors affecting color development. Similarly, Roy and Datta (2025) used MARS as an alternative model in a coupled simulation optimization framework for managing saltwater intrusion in coastal groundwater systems. Their results show that MARS has high predictive accuracy and significantly reduced computational requirements compared to traditional density-driven flow and solute transport simulations.

Each algorithm offers unique strengths for predicting buoyant jet behavior. ELM is valued for its speed and efficiency, making it particularly useful when real-time or large-scale simulations are required. MARS is explored for its interoperability and flexibility in handling both linear and nonlinear relationships, allowing it to model complex interactions between parameters with ease, while maintaining interpretability in its results. ANFIS is known for its ability to combine the benefits of both fuzzy logic and neural networks, making it highly effective for modeling complex, nonlinear relationships. It excels in capturing uncertainty and imprecision in data, which makes it well-suited for scenarios where traditional models might struggle, particularly in cases where expert knowledge or linguistic variables are involved. ANFIS provides the flexibility to adapt its structure based on input-output relationships, making it ideal for tasks where interpretability and accuracy are both crucial. By evaluating these algorithms, the goal is to identify which provides the most accurate and efficient predictions for vertical confined buoyant jets under varying conditions.

3.2 methodology

3.2.1 Data

In Figure 2.9, a positively confined buoyant jet is discharged from the middle jet hole. The velocity is represented by u_j, the density of the ambient water is defined by ρ_a, and the density of the jet water is represented by ρ_j. When $\rho_j < \rho_a$, the jet water rises. D is the diameter of the jet, and D_r is the diameter of the riser tube. In addition, one of the most important parameters in dense jet analysis is the jet density Froude number, which is related to density and jet velocity and is calculated as equations 3.1-3.2:

$$Fr = \frac{u_j}{\sqrt{g'D}} \tag{3.1}$$

$$g' = g\frac{\rho_a - \rho_j}{\rho_a} \tag{3.2}$$

Where g' is the modified gravitational acceleration, and g is gravitational acceleration. For numerical modeling, the mass and momentum equations for an incompressible fluid can be used as described by Kheirkhah Gildeh et al. (2015)

The initial dilution characteristics are different from those of a free buoyancy jet due to lateral constraints, which inhibit the diffusion of the jet and the intrusion of ambient water into the jet. Therefore, when predicting the initial dilution, the effect of lateral constraints should also be considered and expressed in terms of jet concentration S. The jet concentration is mainly affected by Fr and confinement. Confinement is related to D_r / D, H_r / D, and Z / D, so the following function can be used (Yan and Mohammadian, 2017).

$$S = \frac{C - C_a}{C_j - C_a} = f(Fr, \frac{D_r}{D}, \frac{H_r}{D}, \frac{Z}{D}) \tag{3.3}$$

Where C is the concentration at a point, C_a is the concentration of the ambient water, C_j is the inlet jet concentration, and Z is the vertical displacement of a cross-section. The cross-sectional concentrations of the confined vertical buoyant jet at different heights can be fitted to a Gaussian distribution. The concentration field can be easily estimated if the centerline concentration C_c at a cross-section is known, where r represents the radial distance from the centerline. Thus, the jet centerline concentration C_c serves as the key parameter in characterizing the dilution properties.

The geometric parameters D_r / D and H_r / D of the transverse constraint can be combined into a single parameter β, defined as equation 3.4:

$$\beta = \frac{H_r / D}{(D_r / D) - 1} \tag{3.4}$$

The experiments were conducted in the Laser Laboratory of the Hydraulics Laboratory at the University of Ottawa using a glass test tank with lateral confinement provided by riser tubes of varying diameters. A vertical buoyant jet was discharged through a centrally positioned nozzle, and the concentration field was measured using a laser-induced fluorescence (LIF) technique. A range of jet and confinement parameters was systematically varied, including Froude number (3 – 35), Reynolds number (1474 – 4421), jet velocity (0.123 – 0.737 m/s), jet temperature (28 – 59.69 °C), reduced gravity (0.0286 – 0.1448 m/s^2), and jet density (983.72 – 995.19 kg/m^3). The ambient water temperature and density were maintained at 22 °C and 998.1 kg/m^3, respectively. Nozzle diameters of 6 mm and 12 mm were used in combination with riser diameters of 18 mm, 31 mm, and 51 mm, resulting in pipe diameter ratios ranging from 0.118 to 0.5. Unlike a free jet discharged into an unbounded ambient environment, the lateral confinement in this study alters entrainment and mixing characteristics. The confinement parameter varied from 35 to 90, and the confinement index ranged from 1.33 to 15.

A total of 2,344 data samples were obtained from the experiments. Of these, 70% were randomly selected for model training and the remaining 30% for testing. The random division was performed using MATLAB's random permutation function to ensure unbiased evaluation. These data points were obtained by extracting concentration values at multiple vertical positions (Y/D) from each experimental run, which allowed a relatively small number of physical experiments to generate a rich dataset for machine learning model training. Accordingly, the centerline dimensionless concentration can be expressed as a function of Fr, Re, β, and Y/D. Therefore, one of the main goals of this study is to determine the most favorable model for predicting jet concentration based on the correlation between these dimensionless parameters, and to assess the performance of ANFIS, ELM, and MARS models. All models were developed using MATLAB, and the input variables and data ranges are summarized in Table 3.1.

Table 3.1. Experimental parameters.

Parameter	Formula	Value
Jet Froude number	$Fr = U_j / \sqrt{g'D}$	3 - 35
Jet Reynolds number	$\mathrm{Re} = U_j D / \nu$	1474 - 4421
Jet velocity	U_j	0.123 - 0.737
Jet temperature	T_j	28 - 59.69 $^\circ C$
Jet reduced gravity	$g' = g \dfrac{\rho_j}{\rho_j - \rho_a}$	0.0286 - 0.1448 m/s^2
Jet density	ρ_j	983.72 - 995.19 kg/m^3
Test tank temperature	T_a	22 $^\circ C$
Test tank density	ρ_a	998.1 kg/m^3
Water kinematic viscosity	ν	$1\times10^{-6} m^2/s$
Nozzle diameter	D	6, 12 mm
Riser tube diameter	D_r	18, 31, 51 mm
Confinement parameter	Y/D	35 - 90
Pipe diameter ratio	D_r/D	2 - 8.5
Imager spatial resolution	Pixel(width)* Pixel(length)	1080×1920
confinement index	$\beta = \dfrac{H_r/D}{(D_r/D)-1}$	1.33 - 15

3.2.2 Adaptive Neuro-Fuzzy Inference System (ANFIS)

The adaptive neuro-fuzzy inference system (ANFIS) is a hybrid modeling approach that integrates the fuzzy logic framework with the learning capability of artificial neural networks (Jang, 1993; Gholami et al., 2018). It is particularly effective for modeling complex and nonlinear relationships. ANFIS adopts a Takagi–Sugeno–Kang (TSK) type fuzzy inference structure, in which the rules are typically expressed as:

$$\text{Rule}\, l: \text{If}\, x_1 \text{ is } A_1^l \text{ and } x_2 \text{ is } B_1^l \Rightarrow y^l = w_0^l + w_1^l x_1 + w_2^l x_2$$

The system consists of the following five layers, as illustrated in Figure 3.1:

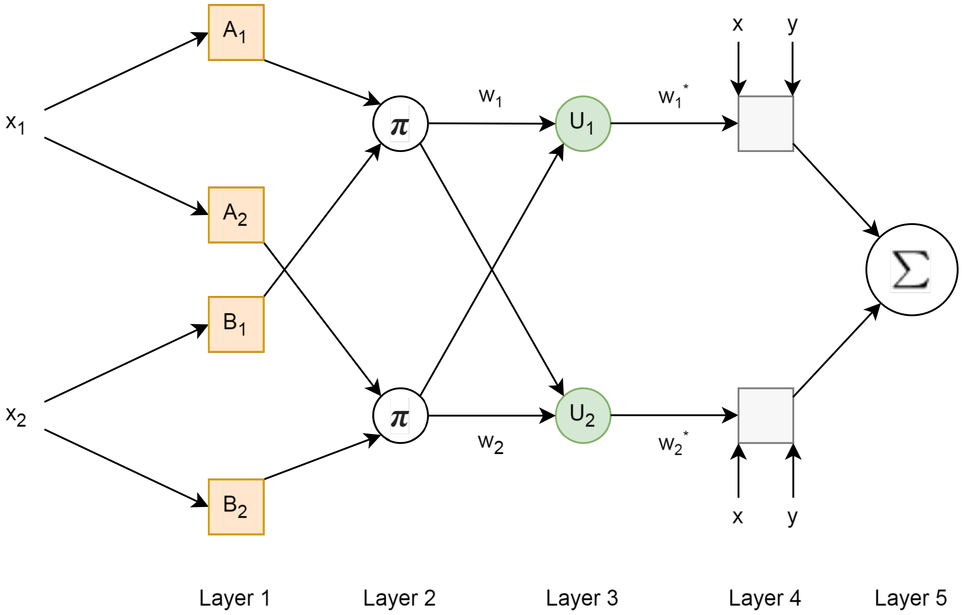

Figure 3.1. Architecture of the Adaptive Neuro-Fuzzy Inference System (ANFIS).

Layer 1 (Input fuzzification): Computes the degree to which each input belongs to a fuzzy set. For example, Gaussian membership functions are commonly used:

$$\mu_{A_j}(x_i) = \exp\left(-\frac{(x_i - c_j)^2}{2\sigma_j^2}\right) \tag{3.5}$$

Layer 2 (Rule layer): Calculates the firing strength of each rule by combining the membership degrees:

$$w^l = \mu_{A_1^l}(x_1) \cdot \mu_{A_2^l}(x_2) \tag{3.6}$$

Layer 3 (Normalization): Normalizes the firing strengths:

$$\overline{w}^{l} = \frac{w^{l}}{\sum_{k=1}^{R} w^{k}} \tag{3.7}$$

Layer 4 (Rule outputs): Computes the rule output based on the normalized firing strength and the linear output function:

$$\overline{w}^{l} \cdot y^{l} = \overline{w}^{l} (w_0^l + w_1^l x_1 + w_2^l x_2) \tag{3.8}$$

Layer 5 (Aggregation): Aggregates the outputs of all rules to produce the final output:

$$y = \sum_{l=1}^{R} \overline{w}^{l} \cdot y^{l} = \sum_{l=1}^{R} \overline{w}^{l} \cdot (w_0^l + w_1^l x_1 + w_2^l x_2) \tag{3.9}$$

This basic ANFIS architecture provides a flexible and interpretable modeling approach that is capable of capturing both linear and nonlinear relationships in data without requiring an explicit mathematical model of the system.

3.2.3 Extreme Learning Machine (ELM)

The extreme learning machine (ELM) is a new learning algorithm based on the single hidden layer feedforward neural network (SLFNN). It was first proposed by Huang et al. in 2006 (Huang et al., 2006). A notable feature of this method is that the parameters of its hidden layer nodes can be randomly generated and optimized with a small amount of adjustment. Compared with traditional neural networks, ELM only needs to set the main free parameter, the connection weight between the hidden layer and the output layer (Huang et al., 2015). Since ELM is constructed as a single hidden layer structure, it effectively avoids many common problems of gradient descent methods, such as learning rate setting, slow convergence speed, and falling into local optimality. ELM uses random allocation of input layer weights and analytical calculation of output weights to achieve efficient approximation of the objective function (Huang et al., 2006).

The extreme learning machine (ELM) network consists of three parts: input layer, hidden layer, and output layer. The input layer is responsible for receiving and transmitting input feature variables to provide raw data support for which acts as an intermediary between input and output to map and transform information. The signal processed by the hidden layer is passed to the output layer, which is used to express the prediction results or response variables and is the convergence point of the final output results (Ebtehaj et al. 2018), as illustrated in Figure 3.2.

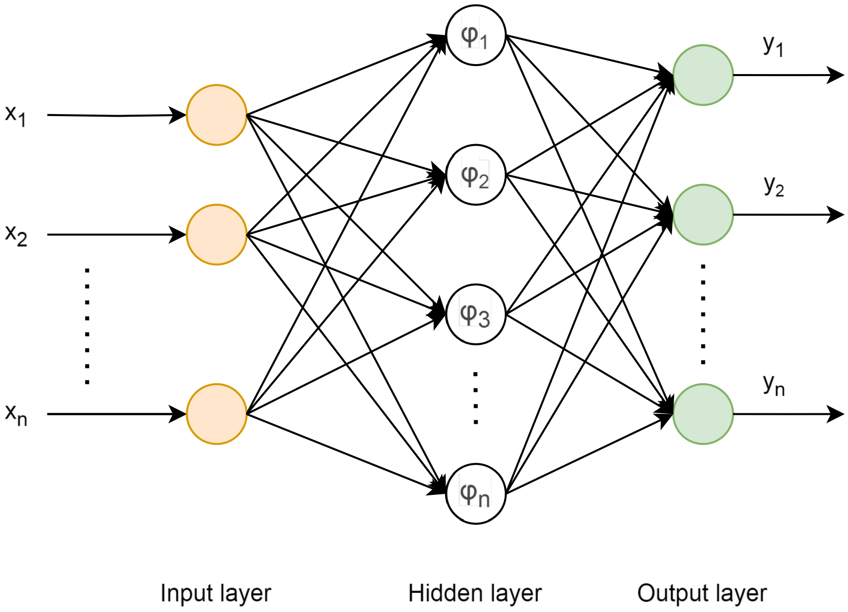

Figure 3.2. Architecture of the Extreme Learning Machine (ELM).

The mathematical formulation of the Extreme Learning Machine is based on the single-hidden-layer feedforward neural network (SLFNN) structure. For a given training dataset (x_i , t_i),where $x_i \in R^n$ is the input vector and $t_i \in R^m$ is the target output, the output function of the SLFNN with LLL hidden nodes can be expressed as:

$$f_L(x) = \sum_{i=1}^{L} \beta_i G(a_i, b_i, x) \tag{3.10}$$

where a_i and b_i are the input weights and biases of the i th hidden node, β_i is the output weight connecting the hidden node to the output layer, and $G(a_i, b_i, x)$ denotes the activation function output for the input x (Huang et al., 2006; Liang et al., 2006).

For additive hidden nodes, such as those using sigmoid or sine functions, the activation can be defined as:

$$G(a_i, b_i, x) = g(a_i \cdot x + b_i) \tag{3.11}$$

The output function for all N training samples can be rewritten in matrix form:

$$H\beta = T \tag{3.12}$$

where H is the hidden layer output matrix, β is the vector of output weights, and T is the target output matrix. The output weights are obtained using the Moore-Penrose generalized inverse of H:

$$\beta = H + T \tag{3.13}$$

This analytical solution allows ELM to avoid iterative tuning, significantly accelerating the training process while preserving the universal approximation capability of SLFNNs (Huang et al., 2006; Ebtehaj et al., 2018).

3.2.4 Multivariate Adaptive Regression Splines (MARS)

The multivariate adaptive regression spline (MARS) model is a nonparametric regression technique first introduced by Friedman (1991), which combines linear and nonlinear regression by fitting piecewise linear splines to data. Unlike traditional regression methods, MARS does not require prior knowledge of the functional relationships between input and output variables. It automatically detects variable interactions and nonlinearities, making it a powerful tool for modeling complex systems in hydraulic and hydrologic applications (Mohanta and Patra, 2019).

The general formulation of a MARS model is:

$$y = c_0 + \sum_{i=1}^{N} c_i \prod_{j=1}^{K_i} F_{ji}(x_{v(j,i)}) \tag{3.14}$$

Where y is the output variable, c_0 is the intercept, c_i are the coefficients of the basis functions F_{ji}, $x_{v(j,i)}$ is the input variable involved in the j-th factor of the i-th term, F_{ji} are truncated power spline basis functions.

The basis functions take the form:

$$\begin{aligned} F_{ji}^{+}(x - t_{ji}) &= (x - t_{ji})_{+}^{q} = \begin{cases} (x - t_{ji})^{q}, x > t_{ji} \\ 0, \text{otherwise} \end{cases} \\ F_{ji}^{-}(x - t_{ji}) &= (t_{ji} - x)_{+}^{q} = \begin{cases} (t_{ji} - x)^{q}, x < t_{ji} \\ 0, \text{otherwise} \end{cases} \end{aligned} \tag{3.15}$$

Here, t_{ji} denotes the knot or breakpoint of the spline. The model construction involves a forward step (adding basis functions to reduce training error) and a backward pruning step (removing less effective terms using criteria such as residual sum of squares (RSS) and generalized cross-validation (GCV)) to avoid overfitting (Friedman, 1991; Mohanta and Patra, 2019).

3.2.5 Statistical Analysis

To evaluate the predictive accuracy of the developed machine learning models, including ANFIS, ELM, and MARS, a set of commonly used statistical performance indicators were applied. These include the Pearson Coefficient of Correlation (R²), Root Mean Squared Error (RMSE), Mean Absolute Error (MAE), and Mean Absolute Relative Error (MARE). These metrics provide a comprehensive assessment of the agreement between predicted and experimentally observed values. The formulas used for calculation are as follows:

$$R^2 = \left(\frac{\sum_{i=1}^{N} (P_O^i - \overline{P_O}) \sum_{i=1}^{N} (P_M^i - \overline{P_M})}{\sqrt{\sum_{i=1}^{N} (P_O^i - \overline{P_O})^2 \sum_{i=1}^{N} (P_M^i - \overline{P_M})^2}} \right)^2 \tag{3.18}$$

$$RMSE = \sqrt{\frac{1}{N} \sum_{i=1}^{N} (O_i - P_i)^2} \tag{3.19}$$

$$MAE = \frac{1}{N} \sum_{i=1}^{N} \left| O_i - P_i \right| \tag{3.20}$$

$$MARE = \frac{\sum_{i=1}^{N} \left| O_i - P_i \right|}{\sum_{i=1}^{N} O_i} \tag{3.21}$$

P_i is the predicted value generated by the machine learning model, O_i is the observed value obtained from LIF experiments, $\overline{O}$ is the mean of the observed values, and N is the total number of data samples.

3.3 results and discussion

The accuracy of the ANFIS, ELM, and MARS models was systematically evaluated based on statistical metrics and visual comparisons between predicted and observed dimensionless concentration data. ANFIS provided the most accurate predictions overall, characterized by the highest coefficient of correlation (R² > 0.91) and the lowest error metrics (RMSE, MAE, and MARE), as shown in Table 3.2. ELM also achieved strong predictive performance, showing slightly lower but still competitive accuracy. Although the MARS model exhibited the greatest difference in predictive accuracy among the three, its strength lies in its interpretability, as it generates explicit mathematical equations describing the relationships between parameters.

Table 3.2. Statistical performance indicators of ANFIS, ELM and MARS models on the test set

Model	R²	RMSE	MAE	MARE
ANFIS	0.9078	0.0586	0.0399	0.0746
ELM	0.8942	0.0628	0.0451	0.0842
MARS	0.8200	0.0819	0.0606	0.1034

The agreement between predicted and observed concentrations is illustrated by the scatterplot shown in Figure 3.3. The ANFIS model predictions are very close to the 1:1 reference line, suggesting a high degree of reliability across a wide range of conditions. The ELM predictions, while exhibiting a small amount of dispersion, remain robust and reliable across most of the dataset. The MARS predictions, while showing significant dispersion at extreme concentration values, still provide valuable insights due to their transparency and ease of interpretation. their transparency and ease of interpretation, they can still provide valuable insights.

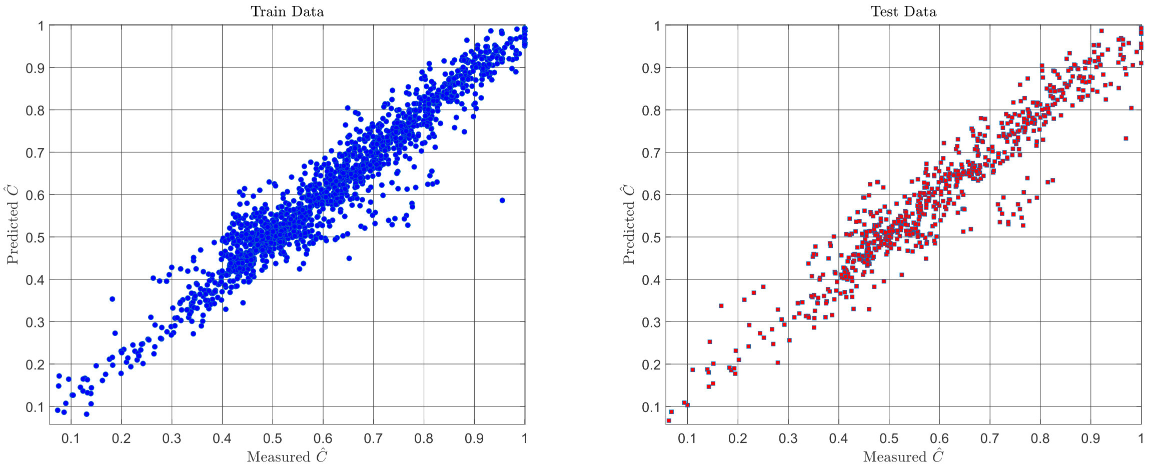

(a) (b)

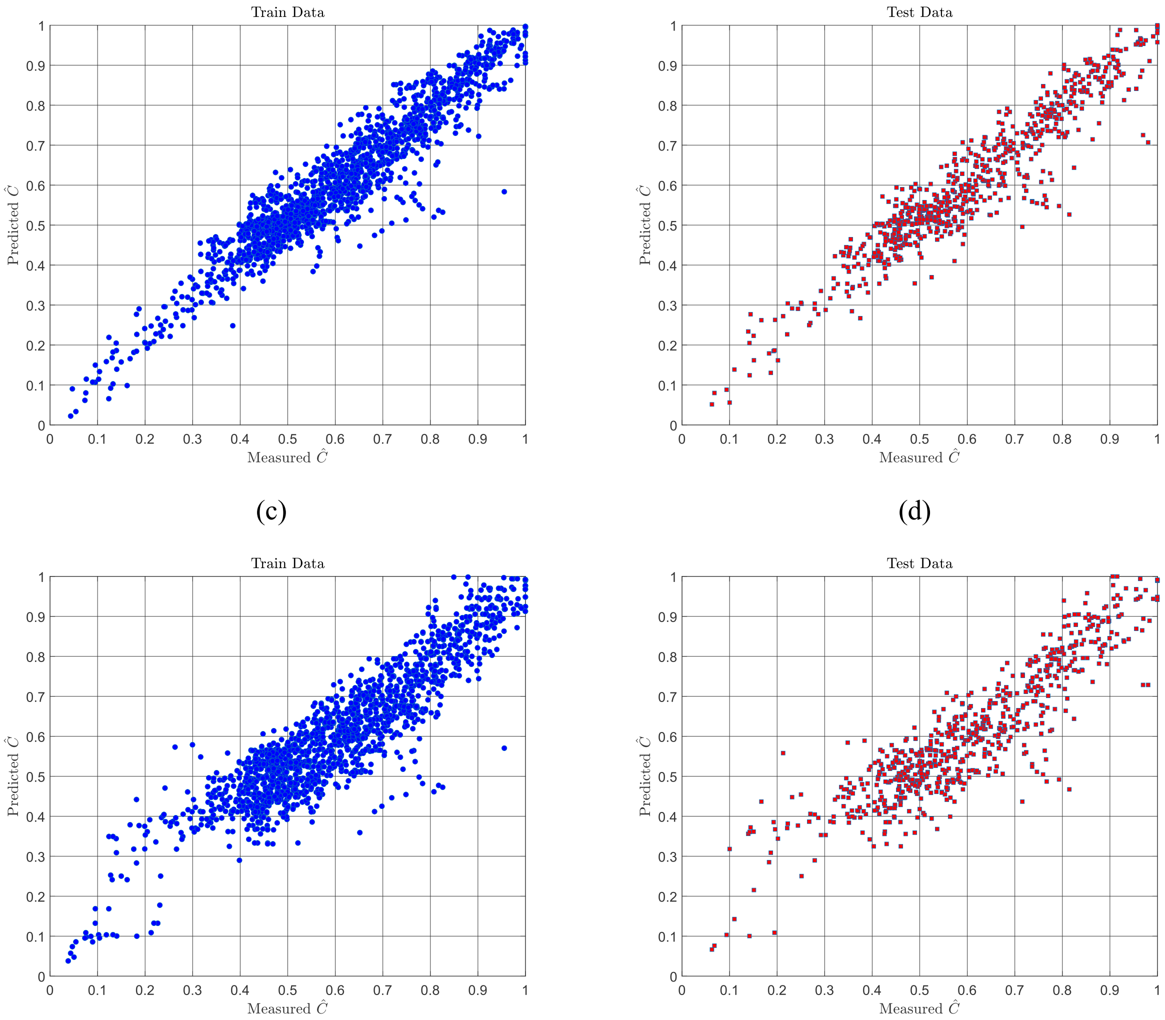

(c) (d)

(e) (f)

Figure 3.3. Scatter plots illustrating the relationship between predicted and actual output values for the ANFIS, ELM, and MARS models: (a) ANFIS model – training data; (b) ANFIS model – testing data; (c) ELM model – training data; (d) ELM model – testing data; (e) MARS model – training data; (f) MARS model – testing data.

The residual distributions depicted in Figure 3.4 further support these observations, providing additional insight into prediction accuracy and error fluctuations. ANFIS residuals are narrowly concentrated around zero, suggesting minimal systematic biases. ELM residuals, though slightly broader, remain generally symmetrical, reflecting consistent accuracy. MARS residuals present greater spread and slight asymmetry, indicating regions of systematic prediction errors which may benefit from further model tuning or refined input parameter selection. The error trend plots illustrate how prediction errors vary across sample indices, further highlighting the consistent performance of ANFIS, the stable yet slightly fluctuating performance of ELM, and the greater variability in errors observed with MARS.

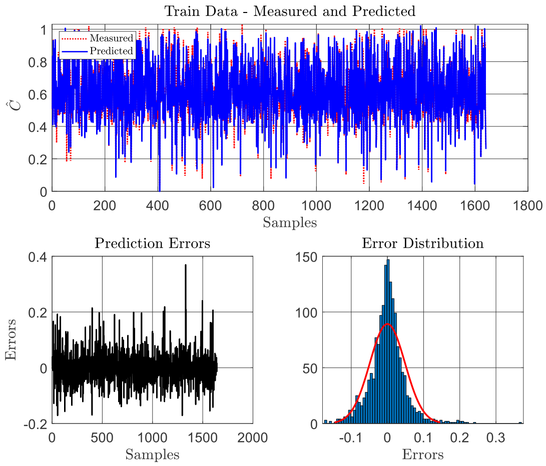

(a)

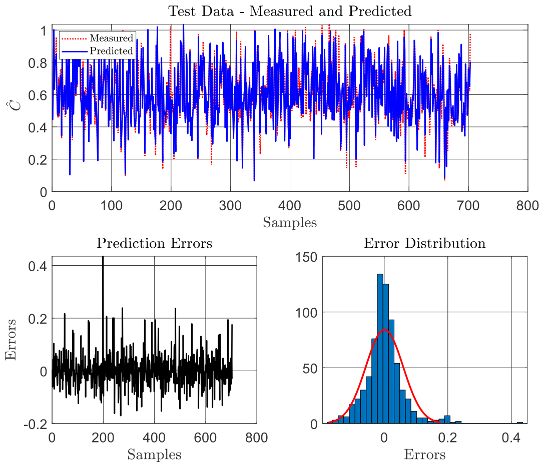

(b)

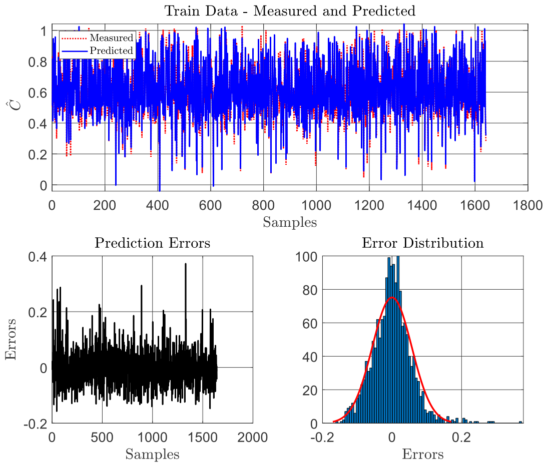

(c)

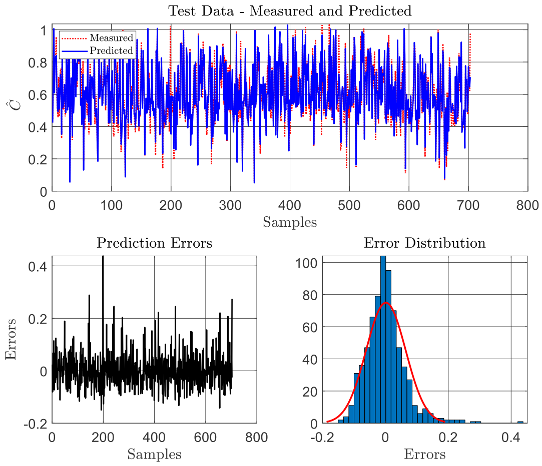

(d)

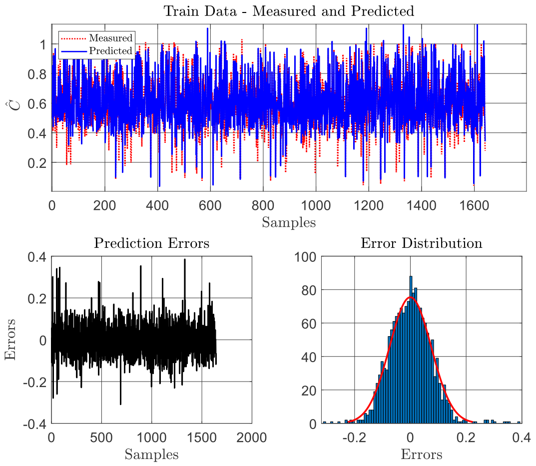

(e)

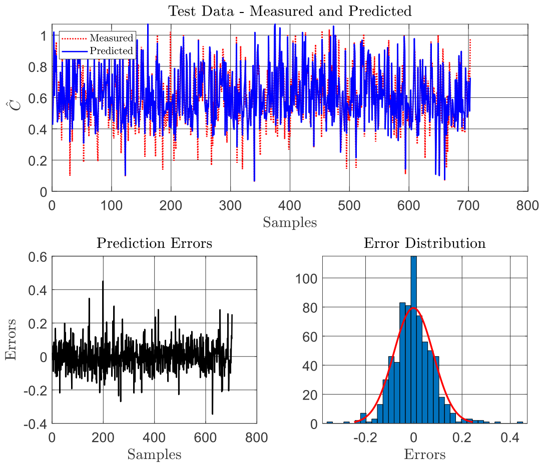

(f)

Figure 3.4. Output performance comparison of ANFIS, ELM, and MARS models, including target vs. output, RMSE, MSE, and error mean plots: (a) ANFIS – training dataset; (b) ANFIS – testing dataset; (c) ELM – training dataset; (d) ELM – testing dataset; (e) MARS – training dataset; (f) MARS – testing dataset.

In terms of computational efficiency, ELM significantly outperforms ANFIS and MARS, benefiting from its non-iterative and rapid training approach. The training time for the ELM model was approximately 50 seconds, which is considerably shorter than that of ANFIS (15 minutes) and slightly faster than MARS (approximately 1.5 minutes), highlighting ELM's computational efficiency. ANFIS, despite its accuracy, requires iterative tuning and substantial computational resources, which may limit its use in time-sensitive applications. MARS offers a balanced compromise, providing reasonable computational speed and explicit equation outputs, which enhances interpretability and facilitates practical engineering applications.

A representative mathematical expression generated by the MARS model is given below, illustrating its explicit interpretability. The model was constructed with 17 basis functions, 33 effective parameters, and a maximum interaction degree of 1. Only two input variables were selected: x_2, representing the Reynolds number (Re), and x_3, representing the vertical distances (Y/D).

It is important to note that certain input variables were not explicitly retained in the final MARS model. This is due to the algorithm's intrinsic feature selection and pruning process, in which a large set of candidate basis functions is initially constructed and then reduced by eliminating terms that do not significantly improve predictive performance, based on a penalized lack-of-fit criterion. In this case, the excluded variables were found to have relatively low standalone predictive contribution, with their effects likely captured indirectly through interactions with the remaining inputs.

To enhance interpretability, the MARS model constructs a set of basis functions (BFs) using hinge functions of the form $\max(0, x - c)$ or $\max(0, c - x)$, where x is an input variable and c is a threshold determined during training. These hinge functions effectively partition the input space, allowing the model to capture localized nonlinear behaviors.

In this case, after generating the 16 basis functions, the MARS algorithm automatically selects a few significant hinge points, favoring 53.5 and 7.5, corresponding to Y/D and the constraint parameter β, respectively. These hinge points have no intrinsic physical significance and serve only as breakpoints for fitting the change in the slope of the response surface. They simply reflect where the regression function is adjusted to better follow the patterns present in the data. These thresholds are automatically identified by evaluating a series of candidate segmentation points and selecting those that best improve the fit of the model.

These basis functions were linearly combined using optimized coefficients to form the final prediction equation:

$$\begin{aligned} y = {} & 3.8671 - 0.0338\times BF_1 + 0.0517\times BF_2 + 0.0031\times BF_3 - 0.0192\times BF_4 - 0.8041\times BF_5 \\ & + 0.2431\times BF_6 - 0.2488\times BF_7 + 0.1266\times BF_8 + 0.0372\times BF_9 + 0.0166\times BF_{10} - 0.0147\times BF_{11} \\ & - 0.1451\times BF_{12} + 0.1580\times BF_{13} - 0.0221\times BF_{14} - 0.3865\times BF_{15} + 0.4274\times BF_{16} \end{aligned}$$

Table 3.3. Functional forms of the basis functions (BFs) constructed by the MARS model.

BF_1	max(0, x_2 − 53.5)	BF_7	max(0, 7.5 − x_3)	BF_{13}	max(0, x_2 − 81)
BF_2	max(0, 53.5 − x_2)	BF_8	max(0, x_3 − 2.3981)	BF_{14}	max(0, 62.5 − x_2)
BF_3	max(0, 3.5971 − x_3)	BF_9	max(0, 63.5 − x_2)	BF_{15}	max(0, 5 − x_3)
BF_4	max(0, 78.5 − x_2)	BF_{10}	max(0, x_2 − 47.5)	BF_{16}	max(0, x_3 − 4.7468)
BF_5	max(0, x_3 − 1.5385)	BF_{11}	max(0, x_2 − 67.5)		
BF_6	max(0, x_3 − 7.5)	BF_{12}	max(0, x_2 − 80)		

Overall, while ANFIS is identified as the most robust model for accurate predictions, MARS provides valuable interpretative benefits due to its explicit mathematical formulation, and ELM stands out in terms of computational efficiency. The choice among these models thus depends on specific project requirements, including the need for interpretability, computational speed, and prediction accuracy.

3.4 conclusion

In this study, three machine learning models - Adaptive Neuro-Fuzzy Inference System (ANFIS), Extreme Learning Machine (ELM), and Multivariate Adaptive Regression Spline (MARS) - are comparatively analyzed to estimate the transversely confined vertical buoyancy jet of centerline dimensionless concentrations. The models were trained and tested using a data set of 2,344 experimental samples under different Froude number and confinement index conditions. The performance of each model was evaluated using standard statistical metrics such as R^2, RMSE, MAE and MARE.

All three models showed acceptable predictive power in the estimation task. Among them, ANFIS performed the best in all statistical metrics with the highest accuracy while taking a moderate amount of time to train. The ELM model produced competitive results with a slightly lower accuracy than ANFIS but required the least amount of computational time. The MARS model, while having the lowest predictive accuracy, had a clear mathematical expression that was easy to interpret and easy to integrate into a real-world application.

All models were trained in less than twenty minutes on an Intel Core i7 10th-generation processor, indicating that these methods are computationally inexpensive and practically feasible. Although ANFIS proved to be the most accurate and ELM the most efficient, MARS remains a strong candidate for modeling in scenarios where interpretability is critical. Future research may involve blending these models or applying them to more complex boundary conditions to improve their generality and robustness in practical fluid dynamics modeling applications.

Chapter 4 conclusion and recommendations

This thesis combines to experimental methods, computational fluid dynamics (CFD) simulations, and machine learning techniques to provide an investigation of the properties of vertically confined buoyant jets and their prediction models. The study is divided into two main parts: the first part includes laboratory experiments and numerical simulations, while the second part focuses on the application and evaluation of various machine learning methods to improve prediction accuracy and computational efficiency.

The experimental study utilizes the laser-induced fluorescence (LIF) technique to capture detailed and accurate concentration fields in different laterally constrained scenarios. These experimental observations provide reference data for a range of computational studies and are simulated using the OpenFOAM software platform. In addition, three Reynolds-averaged Navier-Stokes (RANS)-based turbulence models (i.e., the standard k-ε model, the RNG k-ε model, and the SST k-ω model) are evaluated based on the experimental data for multiple jet configurations.

Among the turbulence models evaluated, the standard k-ε model consistently exhibits good accuracy and reliability with very high R^2 values (typically exceeding 0.99) and low normalized root mean square error (NRMSE) values. This robustness makes the standard k-ε model particularly suitable for practical engineering applications, especially where strong lateral constraints and complex mixing phenomena are involved.The RNG k-ε model also provides reasonable results, showing good predictive power in general, but with slight variations in different scenarios.The SST k-ω model shows reasonable predictive performance, but is more sensitive to specific flow conditions and tends to underestimate the projected flow during the initial mixing phase and tends to underestimate concentrations near the jet centerline. Nevertheless, its predictions improve further downstream, indicating its potential applicability under certain conditions.

The lateral concentration distributions at vertical distances (Y/D) of 20 and 45 further confirm these findings, highlighting a reasonable degree of agreement between numerical simulations and experimental results for both the standard and RNG k-ε models. In contrast, the SST k-ω model exhibits greater variability, especially in complex or highly constrained flow scenarios such as Case A2. In addition to this, further validation using additional highly constrained test scenarios

(Case C3) confirms that all three turbulence models perform reasonably under strongly constrained conditions, with the standard k-ε model again showing a better degree of agreement with the experimental observations.

In the control of experiments and simulations, the dual metric assessment using R^2 and NRMSE improves the reliability of the performance assessment,
To address computational limitations and further improve prediction efficiency, this thesis evaluates three machine learning models: the Adaptive Neuro-Fuzzy Inference System (ANFIS), the Extreme Learning Machine (ELM), and the Multivariate Adaptive Regression Spline (MARS). These models were developed based on experimental datasets and trained quickly (less than 20 minutes per model) using Intel Core i7 10th generation processors, demonstrating their utility in real-time and large-scale prediction applications.

Among them, ANFIS has the highest prediction accuracy, as evidenced by consistently high R^2 values and significantly lower RMSE , MAE,MARE, which proves its ability to effectively model complex nonlinear jet dynamics.ELM exhibits excellent computational efficiency, fast training speed and good prediction performance for scenarios where fast response is critical. At the same time, MARS stands out for its interpretability, providing explicit mathematical expressions through basis functions such as $\max(0, x_2 - 53.5)$ and $\max(0, x_3 - 7.5)$.

In light of these results, several recommendations were made to support future research directions. While the current study provides valuable insights into model performance under selected conditions, further experimental and numerical cases are necessary to determine which turbulence or machine learning model performs best across a broader range of scenarios.

Experiments incorporating Particle Image Velocimetry (PIV) techniques should be conducted to capture detailed velocity fields. These experimental datasets are critical for validating simulation results and improving model fidelity, especially in capturing dynamic three-dimensional flow features that are difficult to observe through numerical methods.

Advancing turbulence modeling is another important area. Combining techniques such as Large Eddy Simulation (LES) or hybrid RANS-LES methods allows for more accurate characterization of flow structure and unsteady turbulent behavior. Although computationally intensive, these models are better suited to capture the transient and complex features of buoyant jets.

Further development of machine learning methods, especially parameter optimization for MARS, is encouraged. With enhanced configurations, the MARS model can yield more accurate and physically interpretable predictions.

References

Amidu, M. A., Addad, Y., Riahi, M. K., & Abu-Nada, E. (2021). Numerical investigation of nanoparticles slip mechanisms impact on the natural convection heat transfer characteristics of nanofluids in an enclosure. *Scientific Reports*, *11*(1), 15678–15678. https://doi.org/10.1038/s41598-021-95269-z

Anmala, J., & Turuganti, V. (2021). Comparison of the performance of decision tree (DT) algorithms and extreme learning machine (ELM) model in the prediction of water quality of the Upper Green River watershed. *Water Environment Research*, *93*(11), 2360–2373. https://doi.org/10.1002/wer.1642

Coolen, M. C. J., Kieft, R. N., Rindt, C. C. M., & van Steenhoven, A. A. (1999). Application of 2-D LIF temperature measurements in water using a Nd : YAG laser. *Experiments in Fluids*, *27*(5), 420–426. https://doi.org/10.1007/s003480050367

Dastgheib, S. A., Musavi-Jahromi, S. H., & Nowroozpour, A. R. (2013). Predicting Hydraulic Properties of Circular Buoyant Jets in the Static Ambient Flow Using ANN and ANFIS. In *World Environmental and Water Resources Congress 2013* (pp. 1880–1895). https://doi.org/10.1061/9780784412947.184

Ebtehaj, I., Bonakdari, H., Moradi, F., Gharabaghi, B., & Khozani, Z. S. (2018). An integrated framework of Extreme Learning Machines for predicting scour at pile groups in clear water condition. *Coastal Engineering (Amsterdam)*, *135*, 1–15. https://doi.org/10.1016/j.coastaleng.2017.12.012

Englert, D., Zubrod, J. P., Schulz, R., & Bundschuh, M. (2013). Effects of municipal wastewater on aquatic ecosystem structure and function in the receiving stream. *The Science of the Total Environment*, *454–455*, 401–410. https://doi.org/10.1016/j.scitotenv.2013.03.025

Ferrier, A. J., Funk, D. R., Roberts, P. J. W., Van Atta, C., Boyer, D., & Fernando, H. (1993). Application of optical techniques to the study of plumes in stratified fluids. *Dynamics of Atmospheres and Oceans*, *20*(1), 155–183. https://doi.org/10.1016/0377-0265(93)90052-9

Friedman, J. H. (1991). Multivariate Adaptive Regression Splines. *The Annals of Statistics*, *19*(1), 1–67. https://doi.org/10.1214/aos/1176347963

Gosman, A. D., & Simitovic, R. (1986). An experimental study of confined jet mixing. *Chemical Engineering Science*, *41*(7), 1853–1871. https://doi.org/10.1016/0009-2509(86)87065-8

Hipni, A., El-shafie, A., Najah, A., Karim, O. A., Hussain, A., & Mukhlisin, M. (2013). Erratum to: Daily Forecasting of Dam Water Levels: Comparing a Support Vector Machine (SVM) Model With Adaptive Neuro Fuzzy Inference System (ANFIS). *Water Resources Management*, *27*(11), 4113–4113. https://doi.org/10.1007/s11269-013-0406-0

Huang, G., Huang, G.-B., Song, S., & You, K. (2015). Trends in extreme learning machines: A review. *Neural Networks*, *61*, 32–48. https://doi.org/10.1016/j.neunet.2014.10.001

Huang, G.-B., Zhu, Q.-Y., & Siew, C.-K. (2006). Extreme learning machine: Theory and applications. *Neurocomputing (Amsterdam)*, *70*(1), 489–501. https://doi.org/10.1016/j.neucom.2005.12.116

Imanian, H., Hiedra Cobo, J., Payeur, P., Shirkhani, H., & Mohammadian, A. (2022). A Comprehensive Study of Artificial Intelligence Applications for Soil Temperature Prediction in Ordinary Climate Conditions and Extremely Hot Events. *Sustainability*, *14*(13), 8065-. https://doi.org/10.3390/su14138065

Imanian, H., & Mohammadian, A. (2019). Numerical simulation of flow over ogee crested spillways under high hydraulic head ratio. *Engineering Applications of Computational Fluid Mechanics*, *13*(1), 983–1000. https://doi.org/10.1080/19942060.2019.1661014

Issa, R. I., Gosman, A. D., & Watkins, A. P. (1986). The computation of compressible and incompressible recirculating flows by a non-iterative implicit scheme. *Journal of Computational Physics*, *62*(1), 66–82. https://doi.org/10.1016/0021-9991(86)90100-2

Jang, J.-S. R. (1993). ANFIS: adaptive-network-based fuzzy inference system. *IEEE Transactions on Systems, Man, and Cybernetics*, *23*(3), 665–685. https://doi.org/10.1109/21.256541

Jasmine, M., Mohammadian, A., & Bonakdari, H. (2022). On the Prediction of Evaporation in Arid Climate Using Machine Learning Model. *Mathematical and Computational Applications*, *27*(2), 32-. https://doi.org/10.3390/mca27020032

Jirka, G. H. (2007). Buoyant Surface Discharges into Water Bodies. II: Jet Integral Model. *Journal of Hydraulic Engineering (New York, N.Y.)*, *133*(9), 1021–1036. https://doi.org/10.1061/(ASCE)0733-9429(2007)133:9(1021)

Jirka, G. H., & Harleman, D. R. F. (1979). Stability and mixing of a vertical plane buoyant jet in confined depth. *Journal of Fluid Mechanics*, *94*(2), 275–304. https://doi.org/10.1017/S0022112079001038

Jones, G. R., Nash, J. D., Doneker, R. L., & Jirka, G. H. (2007). Buoyant Surface Discharges into Water Bodies. I: Flow Classification and Prediction Methodology. *Journal of Hydraulic Engineering (New York, N.Y.)*, *133*(9), 1010–1020. https://doi.org/10.1061/(ASCE)0733-9429(2007)133:9(1010)

Kheirkhah Gildeh, H., Mohammadian, A., Nistor, I., & Qiblawey, H. (2014). Numerical Modeling of Turbulent Buoyant Wall Jets in Stationary Ambient Water. *Journal of Hydraulic Engineering (New York, N.Y.)*, *140*(6). https://doi.org/10.1061/(ASCE)HY.1943-7900.0000871

Kheirkhah Gildeh, H., Mohammadian, A., Nistor, I., & Qiblawey, H. (2015). Numerical modeling of 30∘ and 45∘ inclined dense turbulent jets in stationary ambient. *Environmental Fluid Mechanics (Dordrecht, Netherlands : 2001)*, *15*(3), 537–562. https://doi.org/10.1007/s10652-014-9372-1

Kisi, O., & Parmar, K. S. (2016). Application of least square support vector machine and multivariate adaptive regression spline models in long term prediction of river water pollution. *Journal of Hydrology (Amsterdam)*, *534*, 104–112. https://doi.org/10.1016/j.jhydrol.2015.12.014

Launder, B. E., & Spalding, D. B. (1974). The numerical computation of turbulent flows. *Computer Methods in Applied Mechanics and Engineering*, *3*(2), 269–289. https://doi.org/10.1016/0045-7825(74)90029-2

Lee, A. W.-T., & Lee, J. H.-W. (1998). Effect of Lateral Confinement on Initial Dilution of Vertical Round Buoyant Jet. *Journal of Hydraulic Engineering (New York, N.Y.)*, *124*(3), 263–279. https://doi.org/10.1061/(ASCE)0733-9429(1998)124:3(263)

Lee, C.-H. (2018). Rough boundary treatment method for the shear-stress transport k - ω model. *Engineering Applications of Computational Fluid Mechanics*, *12*(1), 261–269. https://doi.org/10.1080/19942060.2017.1410497

Menter, F. R. (1993). *ZONAL TWO EQUATION k-w TURBULENCE MODELS FOR AERODYNAMIC FLOWS*. 22.

Millero, F. J., & Huang, F. (2009). The density of seawater as a function of salinity (5 to 70 g kg −1) and temperature (273.15 to 363.15 K). *Ocean Science*, *5*(2), 91–100. https://doi.org/10.5194/os-5-91-2009

Millero, F. J., & Poisson, A. (1981). International one-atmosphere equation of state of seawater. *Deep-Sea Research. Part A. Oceanographic Research Papers*, *28*(6), 625–629. https://doi.org/10.1016/0198-0149(81)90122-9

Mohanta, A., & Patra, K. C. (2019). MARS for Prediction of Shear Force and Discharge in Two-Stage Meandering Channel. *Journal of Irrigation and Drainage Engineering*, *145*(8). https://doi.org/10.1061/(ASCE)IR.1943-4774.0001402

Morelissen, R., Vlijm, R., Hwang, I., Doneker, R. L., & Ramachandran, A. S. (2016). Hydrodynamic modelling of large-scale cooling water outfalls with a dynamically coupled near-field-far-field modelling system. *Journal of Applied Water Engineering and Research*, *4*(2), 138–151. https://doi.org/10.1080/23249676.2015.1099480

Nan-Ying Liang, Guang-Bin Huang, Saratchandran, P., & Sundararajan, N. (2006). A Fast and Accurate Online Sequential Learning Algorithm for Feedforward Networks. *IEEE Transactions on Neural Networks*, *17*(6), 1411–1423. https://doi.org/10.1109/TNN.2006.880583

Nayeem, A., Bonakdari, H., Khalloufi, S., & Aider, M. (2024). *Application of multivariate adaptive regression splines (MARS) for analyzing colorization occurring in the process of lactulose production following lactose electro-activation*. SSRN Preprint. https://ssrn.com/abstract=5155426

Pantzlaff, L., & Lueptow, R. M. (1999). Transient positively and negatively buoyant turbulent round jets. *Experiments in Fluids*, *27*(2), 117–125. https://doi.org/10.1007/s003480050336

Sattar, A. M. A., Ertuğrul, Ö. F., Gharabaghi, B., McBean, E. A., & Cao, J. (2019). Extreme learning machine model for water network management. *Neural Computing & Applications*, *31*(1), 157–169.

https://doi.org/10.1007/s00521-017-2987-7

Schewe, J., Heinke, J., Gerten, D., Haddeland, I., Arnell, N. W., Clark, D. B., Dankers, R., Eisner, S., Fekete, B. M., Colón-González, F. J., Gosling, S. N., Kim, H., Liu, X., Masaki, Y., Portmann, F. T., Satoh, Y., Stacke, T., Tang, Q., Wada, Y., … Kabat, P. (2014). Multimodel assessment of water scarcity under climate change. *Proceedings of the National Academy of Sciences - PNAS*, *111*(9), 3245–3250. https://doi.org/10.1073/pnas.1222460110

Shinneeb, A.-M., Balachandar, R., & Bugg, J. D. (2011). Confinement Effects in Shallow-Water Jets. *Journal of Hydraulic Engineering (New York, N.Y.)*, *137*(3), 300–314. https://doi.org/10.1061/(ASCE)HY.1943-7900.0000306

Tahmooresi, S., Goodarzi, D., Mohammadian, A., & Nistor, I. (2025). LIF measurement of turbulent horizontal dense jets in stagnant ambient. *International Journal of Heat and Mass Transfer*, *244*, 126867-. https://doi.org/10.1016/j.ijheatmasstransfer.2025.126867

Tian, X., & Roberts, P. J. W. (2003). A 3D LIF system for turbulent buoyant jet flows. *Experiments in Fluids*, *35*(6), 636–647. https://doi.org/10.1007/s00348-003-0714-x

Wright, S. J. (1984). Buoyant Jets in Density-Stratified Crossflow. *Journal of Hydraulic Engineering (New York, N.Y.)*, *110*(5), 643–656. https://doi.org/10.1061/(ASCE)0733-9429(1984)110:5(643)

Yakhot, V., & Orszag, S. A. (1986). Renormalization group analysis of turbulence. I. Basic theory. *Journal of Scientific Computing*, *1*(1), 3–51. https://doi.org/10.1007/BF01061452

Yan, X., & Mohammadian, A. (2019). Multigene Genetic-Programming-Based Models for Initial Dilution of Laterally Confined Vertical Buoyant Jets. *Journal of Marine Science and Engineering*, *7*(8), 246-. https://doi.org/10.3390/jmse7080246

Yan, X., & Mohammadian, A. (2017). Numerical Modeling of Vertical Buoyant Jets Subjected to Lateral Confinement. *Journal of Hydraulic Engineering (New York, N.Y.)*, *143*(7). https://doi.org/10.1061/(ASCE)HY.1943-7900.0001307

Zhang, S., Jiang, B., Law, A. W.-K., & Zhao, B. (2016). Large eddy simulations of 45° inclined dense jets. *Environmental Fluid Mechanics (Dordrecht, Netherlands : 2001)*, *16*(1), 101–121. https://doi.org/10.1007/s10652-015-9415-2